Article

A claustrum in reptiles and its role in slow-wave sleep

https://doi.org/10.1038/s41586-020-1993-6

Received: 13 August 2019

Accepted: 12 December 2019

Published online: 12 February 2020

Hiroaki Norimoto[1,6], Lorenz A. Fenk[1,6], Hsing-Hsi Li[1], Maria Antonietta Tosches[1,2], Tatiana Gallego-Flores[1], David Hain[1,3], Sam Reiter[1,4], Riho Kobayashi[1,5], Angeles Macias[1], Anja Arends[1], Michaela Klinkmann[1] & Gilles Laurent[1]✉

The mammalian claustrum, owing to its widespread connectivity with other forebrain structures, has been hypothesized to mediate functions that range from decision-making to consciousness[1]. Here we report that a homologue of the claustrum, identified by single-cell transcriptomics and viral tracing of connectivity, also exists in a reptile—the Australian bearded dragon *Pogona vitticeps*. In *Pogona*, the claustrum underlies the generation of sharp waves during slow-wave sleep. The sharp waves, together with superimposed high-frequency ripples[2], propagate to the entire neighbouring pallial dorsal ventricular ridge (DVR). Unilateral or bilateral lesions of the claustrum suppress the production of sharp-wave ripples during slow-wave sleep in a unilateral or bilateral manner, respectively, but do not affect the regular and rapidly alternating sleep rhythm that is characteristic of sleep in this species[3]. The claustrum is thus not involved in the generation of the sleep rhythm itself. Tract tracing revealed that the reptilian claustrum projects widely to a variety of forebrain areas, including the cortex, and that it receives converging inputs from, among others, areas of the mid- and hindbrain that are known to be involved in wake–sleep control in mammals[4–6]. Periodically modulating the concentration of serotonin in the claustrum, for example, caused a matching modulation of sharp-wave production there and in the neighbouring DVR. Using transcriptomic approaches, we also identified a claustrum in the turtle *Trachemys scripta*, a distant reptilian relative of lizards. The claustrum is therefore an ancient structure that was probably already present in the brain of the common vertebrate ancestor of reptiles and mammals. It may have an important role in the control of brain states owing to the ascending input it receives from the mid- and hindbrain, its widespread projections to the forebrain and its role in sharp-wave generation during slow-wave sleep.

Slow-wave sleep and rapid-eye-movement (REM) sleep are the two main macroscopic components of electrophysiological sleep in mammals and birds[4–6], although some mammals may lack REM sleep[7]. The recent finding of alternating slow-wave and REM sleep in a reptile, the Australian bearded dragon *Pogona vitticeps*[3], suggests that these two modes of sleep may predate the diversification of amniotes 320 million years ago. Sleep in *Pogona* is particularly interesting because the sleep cycle of this reptile is very short (3 minutes or less at room temperature), and is divided equally into slow-wave sleep and REM sleep[3].

The dominant electrophysiological feature of *Pogona* slow-wave sleep is energy in the δ frequency band (around 0–4 Hz), which is caused by the reliable occurrence of sharp waves. Sharp waves typically contain a high-frequency ripple, forming a sharp-wave ripple complex (SWR)[2]. SWRs were recorded from the DVR[8]—the dominant non-cortical pallial domain of sauropsid brains[8–10]. REM sleep, by contrast, is characterized by broad-band energy, measured in the β band (10–40 Hz) in the cortex and DVR[3].

Origin of sharp waves during slow-wave sleep

SWRs occured reliably in the DVR during slow-wave sleep, and slow-wave sleep alternated regularly with REM sleep (Fig. 1a–c, Extended Data Fig. 1), as reported previously[3]. High-frequency ripples (around 70–150 Hz) rode on each sharp wave and contained action potentials. Local field potentials (LFPs) were highly correlated across DVR recording sites (peak correlation 0.74 over 18 h of slow-wave sleep, mean over two animals), but sharp waves that were recorded in the anterior medial pole of the DVR (amDVR) preceded their counterparts in more posterior or more lateral regions by up to 200 ms depending on the spacing between recording sites (Fig. 1d, e, Extended Data Fig. 1g, h), suggesting SWR propagation.

We next recorded from thick anterior transverse, horizontal and parasagittal slices of DVR in artificial cerebrospinal fluid solution (ACSF) (Methods, Extended Data Fig. 2a–f). All configurations produced

[1]Max Planck Institute for Brain Research, Frankfurt am Main, Germany. [2]Department of Biological Sciences, Columbia University, New York, NY, USA. [3]Department of Life Sciences, Goethe University, Frankfurt am Main, Germany. [4]Okinawa Institute of Science and Technology Graduate University, Okinawa, Japan. [5]Department of Neuropharmacology, Graduate School of Pharmaceutical Sciences, Nagoya City University, Nagoya, Japan. [6]These authors contributed equally: Hiroaki Norimoto, Lorenz A. Fenk. ✉e-mail: gilles.laurent@brain.mpg.de

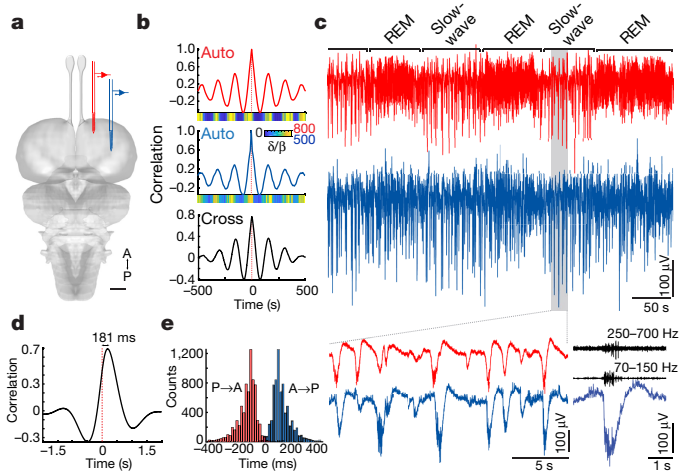

Fig. 1 | SWRs originate in the amDVR in sleeping *Pogona*. **a**, Simultaneous recordings from two sites in the DVR (subcortical). A, anterior; P, posterior. Scale bar, 1 mm. **b**, Auto- and cross-correlations of the δ/β power ratio as function of time from sites in **a**, calculated over 8 h of sleep. Coloured strips show the δ/β ratio over one single 1,000-s stretch of sleep. **c**, Short segment of the data that were analysed in **b** (same trace colours). Bottom left, magnification of a short segment of slow-wave sleep, illustrating SWR coordination and anterior–posterior delay. Bottom right, detail of a SWR and high-pass components (middle and top, black). **d**, Cross-correlation between broadband LFP waveforms (**c**) during 3.42 h of SWS. Reference trace is the anterior recording site: the anterior site leads. **e**, Delay distribution of sharp waves in the anterior (or posterior) DVR triggered on simultaneously recorded posterior (or anterior) DVR. See Methods and Extended Data Fig. 1.

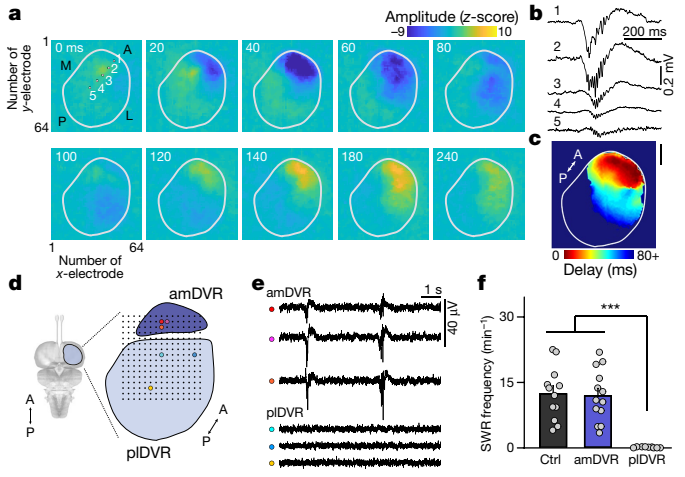

Fig. 2 | SWRs occur spontaneously in DVR slices and originate at the anterior medial pole. **a**–**c**, CMOS–MEA (complementary metal oxide semiconductor–microelectrode array) recordings of SWRs (see also Extended Data Fig. 2) propagating across a horizontal slice of the DVR (outlined). **a**, Instantaneous voltage samples at an interval of 20–60 ms. Squares 1–5 indicate the recording sites shown in **b**. Note the initiation at the anterior pole. L, lateral; M, medial. **b**, SWRs from sites 1–5 in **a**. Note the differences in amplitude and onset time between sites. **c**, Signal latency (relative to the earliest channel) over slice plane (mean of 12 SWRs; same slice as in **a**). Scale bar, 1 mm. **d**–**f**, SWRs in mini-slices. A 252-site microelectrode array, 200-μm pitch. **d**, Thick horizontal slices of DVR were subdivided. **e**, Simultaneous LFPs recorded from coloured sites in **d**. plDVR, posterior lateral DVR. **f**, Mean frequency of SWRs in intact slices (control (ctrl); $n = 12$ slices); amDVR ($n = 13$ mini-slices); and plDVR ($n = 9$ mini-slices). ***$P < 0.001$. P values: control versus amDVR, $P = 1$, $t_{23} = 0.04$; control versus plDVR, $P = 7.2 \times 10^{-6}$; $t_{19} = 6.3$; amDVR versus plDVR, $P = 4.6 \times 10^{-6}$, $t_{19} = 6.3$ (two-sided Bonferroni test). Data are mean ± s.e.m.

spontaneous SWRs that matched those produced in sleep: a biphasic waveform (119 ± 40 ms) with a ripple (around 70–150 Hz) on the trough. SWRs in DVR slices were less frequent than those that occur during slow-wave sleep (12.4 ± 1.8 min^{-1} (12 DVR slices, 10 animals) versus 16.45 ± 0.98 min^{-1} during slow-wave sleep (5 slow-wave sleep epochs, 2 sleeping animals)), although not significantly so ($P = 0.18$, Student's t-test). SWR production in slices was not rhythmically interrupted by REM-sleep-like activity as it is during sleep. We patched 12 DVR neurons (Extended Data Fig. 2g–j) and found that, consistent with sleep data, they typically fired 0–3 action potentials during SWRs and were silent between SWRs. Under voltage clamp ($n = 2$), neurons displayed coincident excitatory and inhibitory input during sharp waves (with excitation dominating in current-clamp mode).

We also used multi-electrode arrays on DVR slices ($n = 3$ brains; Methods). As observed in vivo, SWRs propagated from anterior medial to posterior lateral poles (Fig. 2a–c). The apparent linear velocity of the wave in the slice plane was 39 mm s^{-1}, although propagation contained local angular components. We further divided DVR slices into 'mini-slices' ($n = 13$, Fig. 2d). Only those from the anterior medial pole produced SWRs, and rates did not differ significantly from controls (11.9 ± 1.7 min^{-1}; Fig. 2e, f).

scRNA-seq indicates a claustrum homologue

Using a single-cell RNA sequencing (scRNA-seq) strategy, we previously mapped the main neuronal types of the reptilian pallium[11] and described heterogeneity among glutamatergic cell types in the *Pogona* DVR. To characterize the amDVR, we sampled *Pogona* single cells more deeply and more extensively (Methods). Using unsupervised graph-based Louvain clustering on transcripts from 20,257 cells, we identified 4,054 pallial glutamatergic neurons that formed 29 glutamatergic clusters (Fig. 3a, Extended Data Fig. 3).

We located these clusters in the *Pogona* telencephalon using the expression of cluster-specific markers, which were detected by in situ hybridization and/or immunohistochemistry[11]. Two clusters (19 and 20, Fig. 3a) mapped to the amDVR, as shown by expression of *hpca* (which encodes the calcium-binding protein hippocalcin) and *adarb2* (which encodes an RNA-editing enzyme), among others (Fig. 3b–d). Clusters 19 and 20 corresponded to medial and lateral subdivisions of the amDVR, as shown by expression of the copine-4 (*cpne4*) and nuclear hormone receptor (*rorb*) genes (Fig. 3e, f). When we repeated the mini-slice SWR recordings and labelled those slices afterwards with a hippocalcin antibody, we found that only hippocalcin-positive mini-slices from the anterior medial pole of the DVR generated SWRs (Extended Data Fig. 4).

Some amDVR markers (for example, *gng2*, *synpr* and *rgs12*; Fig. 3b) are known markers of the mammalian claustrum[12]. To explore these molecular similarities further, we used Seurat v.3 to project *Pogona* single-cell transcriptomes onto mouse single-cell transcriptomes[13] on the basis of a joint dimensionality reduction analysis[14] (Methods). About 63% and 75% of amDVR cells (clusters 19 and 20, respectively) projected onto the mouse claustrum transcriptomic cluster (Fig. 3g). This suggests that—consistent with developmental observations[10,15]—the *Pogona* amDVR and the mammalian claustrum are homologous.

To link our transcriptomic and physiological observations, we analysed the expression of genes that encode ion channels and neurotransmitter receptors in pallial glutamatergic clusters (143 genes detected in at least 20% of cells of at least one cluster; Methods). These genes were sufficient to distinguish the amDVR from other glutamatergic clusters (Extended Data Figs. 3, 5), and contained clusters of correlated genes (modules). One module with enriched expression in the amDVR (Fig. 3h) included receptors for noradrenaline, acetylcholine, dopamine and serotonin. In mammals, these neuromodulators influence sleep rhythms and are released by brain nuclei from the hypothalamus to the medulla[4,5,16–18]. Glutamatergic neurons in the amDVR were among the

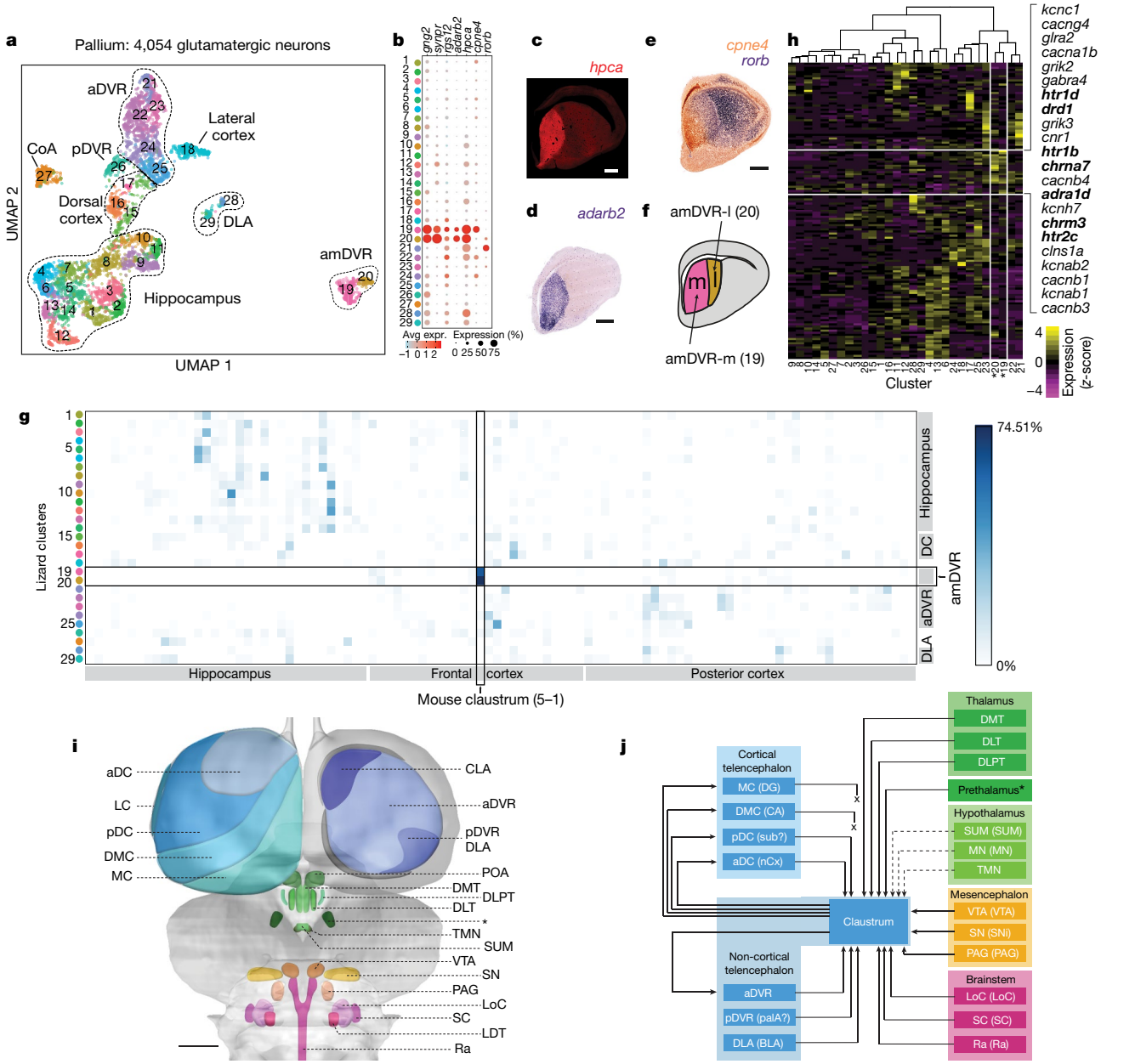

Fig. 3 | scRNA-seq and viral tract tracing show that the amDVR is a reptilian claustrum. a, Uniform manifold approximation and projection (UMAP)[42] representation of single-cell transcriptomes of 4,054 *Pogona* glutamatergic pallial neurons. Cells are colour-coded by cluster (1–29). CoA, cortical amygdala; DLA, dorsal lateral amygdala. See Extended Data Figs. 3, 5. **b**, Expression across clusters of marker genes with high, specific expression in the amDVR (clusters 19, 20). These include markers of the mammalian claustrum. The size of the dot corresponds to the fraction of cells in which the gene is detected and the colour represents the expression level. **c**–**e**, Anterior transverse sections of *Pogona* telencephalon with immunostaining for hippocalcin (*hpca*) (**c**), in situ hybridization for *adarb2* (**d**) and double in situ hybridization with *cpne4* and *rorb* probes (**e**). Scale bars, 500 µm. **f**, Diagram showing the medial (m) and lateral (l) subdivisions of the amDVR. **g**, Transcriptomic similarity between lizard and mouse clusters, measured as the fraction of single-cell transcriptomes that map from *Pogona* to mouse clusters (Methods; mouse data are from a previous study[13]). **h**, Average expression in the *Pogona* clusters of 143 ion-channel and neurotransmitter-receptor genes (Extended Data Fig. 5). Clusters 19 and 20 (marked with an asterisk) correspond, respectively, to the medial and lateral subdivisions of the amDVR shown in **f**. Genes with enriched expression in the amDVR are listed on the right, with relevant neurotransmitter receptor genes in bold. **i**, Schematic of the *Pogona* brain. Forebrain areas (blue) were identified by scRNA-seq and in situ hybridization[11]. Diencephalic (green), mesencephalic (orange) and rhombencephalic (pink) areas were identified by immunohistochemistry and FISH (see Extended Data Fig. 6). aDC, anterior dorsal cortex; CLA, claustrum; DLT, dorso-lateral thalamus; DLPT, dorso-lateral posterior thalamus; DMC, dorso-medial cortex; DMT, dorso-medial thalamus; LC, lateral cortex; LDT, lateral dorsal tegmental nucleus; LoC, locus coeruleus; MC, medial cortex; PAG, periaqueductal grey; pDC, posterior dorsal cortex; POA, preoptic area; Ra, raphe nuclei; SC, subcoeruleus; SN, substantia nigra (SNi for mammals); SUM, supramammillary nucleus; TMN, tuberomammillary nucleus; VTA, ventral tegmental area. The prethalamus is marked with an asterisk. Scale bar, 1 mm. **j**, Summary of claustrum (amDVR) connectivity with areas in **i**, as determined by viral tracing. Arrows with solid lines indicate connections; 'x' indicates an absence of connection (absence of anterograde and retrograde labelling); and arrows with dotted lines indicate tentative connections (due to inconsistent labelling). Claustral projections to the pDVR or DLA were not conclusively tested, as we were not able to inject rAAV2-retro specifically into those small areas. Abbreviations for mammalian homologues are shown in parentheses: BLA, basolateral amygdala; CA, cornu ammonis; DG, dentate gyrus; nCx, neocortex; palA, pallial amygdala; sub, subiculum. The prethalamus is marked with an asterisk, as in **i**.

few types that co-expressed receptors for all four modulators (Extended Data Fig. 5). Hence, the amDVR expresses receptor types that are consistent with a sensitivity to input from circuits that control brain state.

The amDVR is extensively connected

We next mapped the connectivity of the amDVR with areas that have been associated with wake–sleep control in mammals (as suggested by the above data) and asked whether the amDVR connects widely with the rest of the pallium, as the claustrum does in mammals[1,12,19–21]. We identified, where possible, the *Pogona* homologues of mammalian nuclei that are implicated in sleep[4–6]. Relying on anatomical studies in related species (Methods), we used immunohistochemistry and fluorescence in situ hybridization (FISH) to identify and map these nuclei in the *Pogona* diencephalon, midbrain and brainstem (Fig. 3i, Extended Data Fig. 6), together with telencephalic areas mapped by scRNA-seq[11].

We mapped amDVR connectivity by local tracer injections[22], using an adeno-associated virus vector (rAAV2-retro[23]) carrying a fluorescent-protein gene under the CAG or hSyn promoter for (mostly) retrograde labelling (Methods). rAAV2-retro was sometimes co-injected with the (mostly) anterograde tracer AAV2/9-CB7-mCherry-WPRE for injection-site identification. Because they do not cross synapses[23–25], these tracers revealed the direct targets (AAV2/9-CB7) and sources (rAAV2-retro) of the injection site. The results are summarized in Fig. 3j. The names on the left all describe telencephalic structures, for which the input and output connectivity with the amDVR ('claustrum') could be tested. On the right are deeper structures that for anatomical reasons could not be reached for injection. For these structures, connectivity to the claustrum was established only by retrograde labelling from the amDVR, and the question of whether the claustrum projects to those areas will require further investigation and direct demonstration.

The cortical sources of input to the amDVR were the anterior and posterior dorsal cortices (Fig. 3j, Extended Data Fig. 6c). Retrograde and anterograde tracers revealed no direct projections from the dorso-medial cortex (homologue of the hippocampal cornu ammonis (CA)) and medial cortex (homologue of the dentate gyrus (DG)) to the amDVR, even though the amDVR projects to both (Fig. 3j). In the subcortical pallium, the anterior DVR (aDVR) and posterior DVR (pDVR) showed strong projections to the amDVR. The amDVR also received input from the dorsal thalamus (dorso-medial, dorso-lateral and dorso-lateral posterior nuclei), prethalamus, hypothalamus, ventral tegmental area, substantia nigra, the periaqueductal grey in the midbrain, and the locus coeruleus, subcoeruleus and raphe nucleus in the brainstem (Extended Data Fig. 6).

The amDVR projected to the hippocampus (medial cortex and dorso-medial cortex), posterior dorsal cortex (potential subiculum homologue) and anterior dorsal cortex (neocortex homologue)[11]. In the subcortical pallium, projections to the aDVR were dense and extensive, consistent with sharp-wave propagation (Figs. 1, 2). Projections between the amDVR and some of its targets appeared ordered: more lateral amDVR projected to rostral aDVR and central amDVR projected to caudal aDVR. Conversely, input to the amDVR from the cortex (anterior and posterior dorsal cortex) was strongest laterally and weakest medially (absent from dorso-medial and medial cortices, or hippocampus).

Hence, the amDVR is connected with the pallial forebrain and receives input from areas that are implicated in wake–sleep control—consistent with the widespread expression of many receptor genes that are specific to these areas. On the basis of these transcriptomic and anatomical data, we conclude that the amDVR is the reptilian homologue of the mammalian claustrum.

The claustrum homologue in turtles

Having applied similar transcriptomic approaches to those used in *Pogona* to the turtle *T. scripta*[11]—a species on a distant branch of the reptilian tree—we looked for a turtle claustrum. Comparison of transcriptomic data (Methods) yielded four potential clusters in *Trachemys* (Extended Data Fig. 7). Cells in these clusters were located in a region known as the pallial thickening[11,26,27]. Turtle pallial thickening and lizard amDVR are both in the anterior pallium, consistent with their similar developmental origin in anterior lateral pallium[10]; however, turtle pallial thickening is lateral to the aDVR and close to the olfactory cortex, rather than being fused to the rest of the DVR as the claustrum is in *Pogona*. Architectonics also differed: the *Pogona* claustrum is nuclear and composed of isotropically distributed multipolar neurons, whereas turtle pallial thickening forms a curved sheet that extends the anterior dorsal cortex and is traversed from below by lateral geniculate nucleus (LGN) axons en route to the visual cortex[27]. Principal neurons in turtle pallial thickening (revealed after rAAV2-retro injection into the dorso-medial cortex) are pyramid-like, with apical and basal dendrites (Extended Data Fig. 7d). Despite these differences, slices of turtle pallial thickening produced SWRs that led those in the DVR, as in *Pogona*. This pallial thickening therefore appears to be the turtle claustrum, suggesting that a homologue of the claustrum already existed in the common ancestor of amniotes.

Manipulating claustrum activity

We developed a reduced ex vivo preparation of the *Pogona* forebrain, which enabled direct access to the non-cortical pallium after removal of the cortex (Methods). This preparation generated spontaneous SWRs in the claustrum and DVR that were similar to those recorded in vivo during sleep and to those that occur in slices containing both claustrum and DVR (claustrum + DVR) (Extended Data Fig. 8). SWRs occurred continuously but more frequently in the forebrain preparation ($21.6 \pm 5.4\ min^{-1}$, 4 brains) than in slices ($12.4 \pm 1.8\ min^{-1}$, $n = 13$). SWRs in the claustrum led those in the DVR (Extended Data Fig. 8f), with delays similar to those observed during sleep or in slices of claustrum + DVR (11–141 ms, peak mean correlation 0.57, 4 brains). To test the causal role of the claustrum in generating SWRs, we injected tetrodotoxin (TTX) selectively into the claustrum ex vivo ($n = 4$, 3 animals). This resulted in a prolonged silencing of the claustrum, and the concomitant cessation of SWRs in the ipsilateral DVR (Extended Data Fig. 8b–d).

We next generated lesions in one or both claustra in vivo using ibotenic acid (Methods; three animals). Bilateral recordings from the DVR in sleeping lesioned animals revealed that the rhythmic modulation of β-band activity (REM sleep) was unaffected, but that SWRs (characteristic of slow-wave sleep) were eliminated on the side(s) of the lesioned claustrum (Fig. 4a–d, Extended Data Fig. 9). These findings show that the claustrum is required for the production of SWRs in the DVR during slow-wave sleep; that its action is unilateral; and that it is not involved in the alternating sleep rhythm itself.

Because the claustrum receives direct input from areas that are implicated in wake–sleep control in mammals and expresses receptors for their transmitters (Fig. 3j, Extended Data Fig. 5), we tested how sensitive SWR production was to those transmitters[4–6,16]. Dopamine significantly increased the rate of SWR production, whereas acetylcholine and serotonin decreased it (Fig. 4e). We selected serotonin for further experiments. Consistent with tracing data that indicated a serotonergic input from the raphe nuclei, the claustrum contained serotonin-positive fibres (Extended Data Fig. 10a). Serotonin at concentrations of 1 μM or higher suppressed SWRs ($n = 9$ claustrum + DVR slices, 9 animals; Extended Data Fig. 10b). This effect was best mimicked by the serotonin receptor-1D agonist L703,664 (Fig. 4f), consistent with scRNA-seq results (Extended Data Fig. 5). We then superfused slices with caged serotonin (Methods). SWRs were suppressed within seconds of the onset of illumination, and resumed when illumination stopped (Fig. 4g, h).

The mammalian claustrum is hypothesized to have a role in higher cognition[1,28,29] because of its hub-like connectivity[12,30–32]. Direct

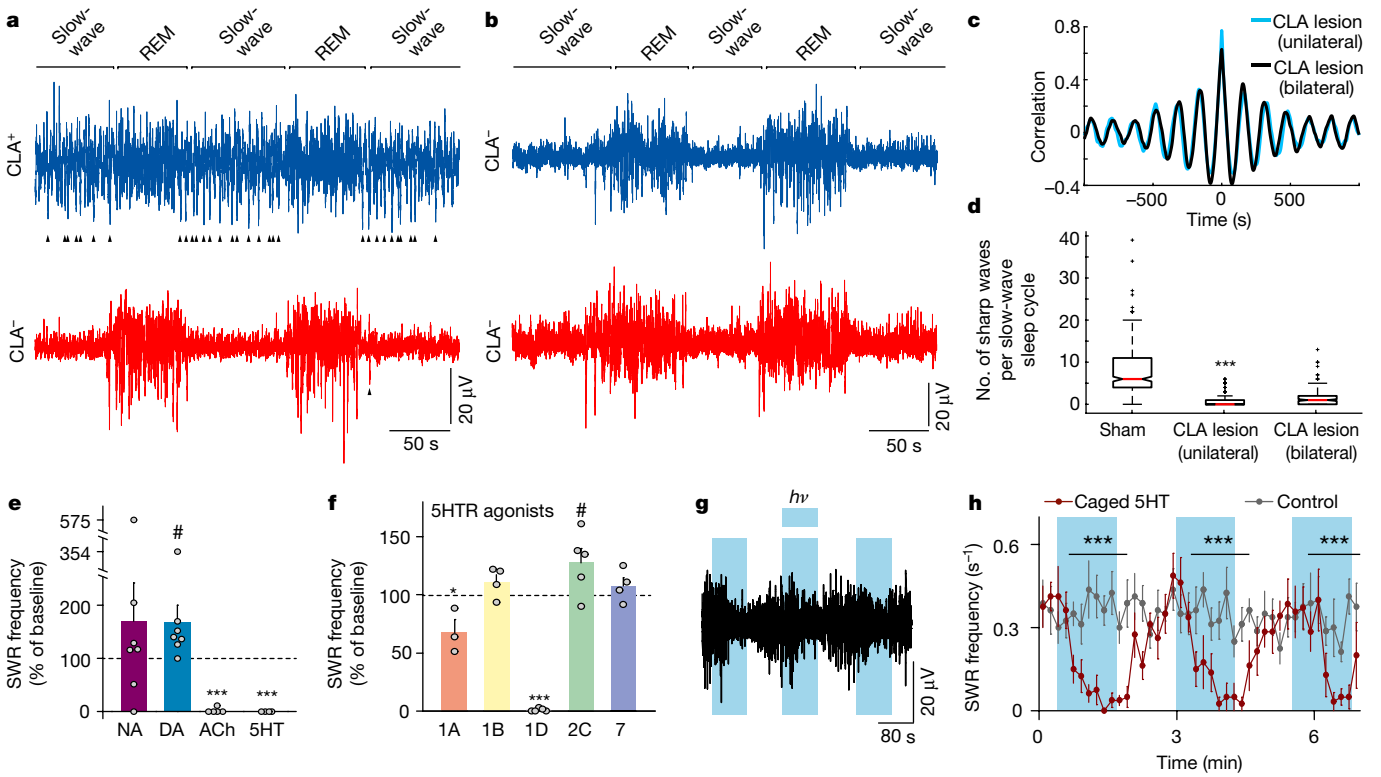

Fig. 4 | SWR production in the DVR depends on claustrum integrity and modulation. a–d, Ibotenic-acid-induced lesions of the claustrum and SWRs in sleeping lizards (see also Extended Data Fig. 9). **a**, Short sleep segment showing LFP (<150 Hz) from left and right DVRs after unilateral claustrum lesion. Sham-lesioned hemisphere (CLA^+) is shown in blue; lesioned hemisphere (CLA^-) is shown in red. The arrowheads indicate sharp waves in the DVR. Sleep rhythm is intact but sharp waves are nearly absent in slow-wave sleep on the lesioned side. **b**, Same as **a**, in a lizard with bilateral lesions of the claustrum. Note the absence of sharp waves. **c**, Cross-correlation of β-band (REM sleep) power across hemispheres in lesioned animals. **d**, Number of sharp waves per slow-wave sleep cycle in sham and claustrum-lesioned hemispheres. ***, significantly different from sham; $P < 1.73 \times 10^{-60}$, $W = 64{,}252$ (Wilcoxon signed-rank test; data from 2 animals, 4 nights, 375 cycles). For details of box plots, see Methods. **e–h**, Experiments in slices of DVR + claustrum or isolated claustrum. **e**, Effects of superfused noradrenaline (NA; 25 μM; $n = 7$;), dopamine (DA) agonist SKF38393 (10 μM; $n = 7$); acetylcholine (ACh) agonist carbachol (50 μM; $n = 5$) and serotonin (5HT; 10 μM; $n = 4$) on the frequency of spontaneous SWRs. **f**, Action of serotonin receptor (5HTR) agonists on the rate of spontaneous SWRs in isolated slices of the claustrum. $n = 3$ experiments (5HTR-1A); $n = 4$ (5HTR-1B); $n = 5$ (5HTR-1D); $n = 5$ (5HTR-2C); $n = 4$ (5HTR-7). ***, * and #, significantly different from baseline; $^{***}P = 8.0 \times 10^{-3}$, $T = 15$ (two-sided Wilcoxon rank-sum test); $^{*}P = 0.04$, $t_4 = -2.9$; $^{\#}P = 0.049$, $t_8 = -2.3$ (paired t-test). Data are mean ± s.e.m. (**e**, **f**). **g**, Light-triggered uncaging of serotonin suppresses spontaneous SWRs in CLA + DVR slices. Blue shading, light on ($h\nu$). **h**, Summary of eight experiments performed as in **g**, with bins of 10 s. Data are mean ± s.e.m. For the control experiments, light pulses were applied to ACSF-superfused slices. ***, experimental bins significantly different from control; $P = 1.5 \times 10^{-4}$, $T = 36$ (two-sided Mann–Whitney rank-sum test).

experimental tests are difficult, however, owing to the anatomy of the claustrum[12,33]. Using scRNA-seq and tract-tracing techniques, we identified a claustrum in two reptiles from distant evolutionary lineages. This result, added to mammalian evidence, suggests that a claustrum probably existed in the common ancestor of amniotes. The claustrum probably derives from the lateral pallium and may correspond to parts of the mesopallium in birds[34,35]. Thus, if the claustrum has a role in higher cognition in mammals, this role may be derived from other functions in a common amniote ancestor. The claustrum assumes different architectonics, which are reflected in neuronal morphology, in two distant reptiles. (Of note, differences also exist between marsupial and placental mammals[36].) Because the claustrum produces SWRs in both reptiles, architectonics probably have little role in SWR generation.

The claustrum participates in the generation and relaying of SWRs that are characteristic of slow-wave sleep in *Pogona*. Given the widespread connectivity of the claustrum and its input from wake–sleep-controlling areas, it may be implicated in coordinating forebrain states during sleep. Early experiments in cats[37] described sleep-like behaviour after (though not during) low-frequency stimulation of the claustrum. These results remain uncertain because selective stimulation of the mammalian claustrum is difficult. More recent results in rodents, using markers of synaptic activity[38], suggest that the claustrum is active during REM sleep. Other studies[39,40] suggest that the claustrum acts to shut down the cortex, through dominant projections onto cortical interneurons. This action would cause a general cortical down-state, as is possibly seen during certain phases of slow-wave sleep[40]. These results collectively suggest a tentative link between the claustrum and sleep in mammals.

During sleep in *Pogona*, SWRs originate in the claustrum and propagate to the rest of the non-cortical pallium—the mammalian homologue of the amygdaloid complex[11]. By virtue of ascending input from areas that control the wake–sleep cycle, the claustrum is ideally positioned to act as a relay for wake–sleep-related states in the forebrain. During sleep the claustrum alternates between SWR production and REM, presumably driven by alternating ascending inputs that are themselves independent of claustrum integrity. Claustrum projections suggest a distributed action on the cortex, hippocampus, amygdala and other areas of the forebrain. SWRs in sleeping *Pogona* in vivo are each correlated with a short phasic inhibition of the cortex (consistent with stimulation experiments (Extended Data Fig. 8) and with results in rodents[39,40]) followed by cortical excitation[3] (consistent with coordination between area CA1 and the medial prefrontal cortex in rodents[41]). The mechanisms that underlie this coordination, and the nature of sleep-related inputs to the claustrum, now require characterization.

Online content

Any methods, additional references, Nature Research reporting summaries, source data, extended data, supplementary information, acknowledgements, peer review information; details of author contributions and competing interests; and statements of data and code availability are available at https://doi.org/10.1038/s41586-020-1993-6.

1. Crick, F. C. & Koch, C. What is the function of the claustrum? *Phil. Trans. R. Soc. Lond. B* **360**, 1271–1279 (2005).
2. Buzsáki, G. Hippocampal sharp wave-ripple: a cognitive biomarker for episodic memory and planning. *Hippocampus* **25**, 1073–1188 (2015).
3. Shein-Idelson, M., Ondracek, J. M., Liaw, H. P., Reiter, S. & Laurent, G. Slow waves, sharp waves, ripples, and REM in sleeping dragons. *Science* **352**, 590–595 (2016).
4. Saper, C. B. & Fuller, P. M. Wake-sleep circuitry: an overview. *Curr. Opin. Neurobiol.* **44**, 186–192 (2017).
5. Weber, F. & Dan, Y. Circuit-based interrogation of sleep control. *Nature* **538**, 51–59 (2016).
6. Scammell, T. E., Arrigoni, E. & Lipton, J. O. Neural circuitry of wakefulness and sleep. *Neuron* **93**, 747–765 (2017).
7. Lyamin, O. I., Manger, P. R., Ridgway, S. H., Mukhametov, L. M. & Siegel, J. M. Cetacean sleep: an unusual form of mammalian sleep. *Neurosci. Biobehav. Rev.* **32**, 1451–1484 (2008).
8. Naumann, R. K. & Laurent, G. in *Evolution of Nervous Systems* Vol. 1 (ed. Kaas, J. H.) 491–518 (Elsevier, 2017).
9. Moreno, N. & González, A. Evolution of the amygdaloid complex in vertebrates, with special reference to the anamnio-amniotic transition. *J. Anat.* **211**, 151–163 (2007).
10. Puelles, L. et al. in *Evolution of Nervous Systems* Vol. 1 (ed. Kaas, J. H.) 519–555 (Elsevier, 2017).
11. Tosches, M. A. et al. Evolution of pallium, hippocampus, and cortical cell types revealed by single-cell transcriptomics in reptiles. *Science* **360**, 881–888 (2018).
12. Wang, Q. et al. Organization of the connections between claustrum and cortex in the mouse. *J. Comp. Neurol.* **525**, 1317–1346 (2017).
13. Saunders, A. et al. Molecular diversity and specializations among the cells of the adult mouse brain. *Cell* **174**, 1015–1030 (2018).
14. Stuart, T. et al. Comprehensive integration of single-cell data. *Cell* **177**, 1888–1902 (2019).
15. Striedter, G. F. The telencephalon of tetrapods in evolution. *Brain Behav. Evol.* **49**, 179–213 (1997).
16. Monti, J. M. Serotonin control of sleep-wake behavior. *Sleep Med. Rev.* **15**, 269–281 (2011).
17. Clément, O., Sapin, E., Bérod, A., Fort, P. & Luppi, P. H. Evidence that neurons of the sublaterodorsal tegmental nucleus triggering paradoxical (REM) sleep are glutamatergic. *Sleep* **34**, 419–423 (2011).
18. Hobson, J. A., McCarley, R. W. & Wyzinski, P. W. Sleep cycle oscillation: reciprocal discharge by two brainstem neuronal groups. *Science* **189**, 55–58 (1975).
19. da Costa, N. M., Fürsinger, D. & Martin, K. A. The synaptic organization of the claustral projection to the cat's visual cortex. *J. Neurosci.* **30**, 13166–13170 (2010).
20. Druga, R. in *The Claustrum: Structural, Functional, and Clinical Neuroscience* (eds Smythies, J. R. et al.) 29–84 (Academic, 2014).
21. Olson, C. R. & Graybiel, A. M. Sensory maps in the claustrum of the cat. *Nature* **288**, 479–481 (1980).
22. Pammer, L. *Explorations of Turtle Cortex Function through Molecular, Optogenetic and Electrophysiological Techniques*. PhD thesis, Goethe Univ. (2017).
23. Tervo, D. G. et al. A designer AAV variant permits efficient retrograde access to projection neurons. *Neuron* **92**, 372–382 (2016).
24. Oh, S. W. et al. A mesoscale connectome of the mouse brain. *Nature* **508**, 207–214 (2014).
25. Harris, J. A., Oh, S. W. & Zeng, H. Adeno-associated viral vectors for anterograde axonal tracing with fluorescent proteins in nontransgenic and Cre driver mice. *Curr. Protoc. Neurosci.* **59**, 1.20.1–1.20.18 (2012).
26. Desan, P. H. in *The Forebrain of Reptiles* (eds Schwerdtfeger, W. K. & Smeets, W. J.) 1–11 (Karger, 1987).
27. Heller, S. B. & Ulinski, P. S. Morphology of geniculocortical axons in turtles of the genera *Pseudemys* and *Chrysemys*. *Anat. Embryol.* **175**, 505–515 (1987).
28. Atlan, G. et al. The claustrum supports resilience to distraction. *Curr. Biol.* **28**, 2752–2762 (2018).
29. Smythies, J., Edelstein, L. & Ramachandran, V. Hypotheses relating to the function of the claustrum. *Front. Integr. Neurosci.* **6**, 53 (2012).
30. Dillingham, C. M., Janowski, M. M., Chandra, R., Frost, B. E. & O'Mara, S. M. The claustrum: considerations regarding its anatomy, functions and a programme for research. *Brain Neurosci. Adv.* **1**, 1–9 (2017).
31. Edelstein, L. R. & Denaro, F. J. The claustrum: a historical review of its anatomy, physiology, cytochemistry and functional significance. *Cell. Mol. Biol.* **50**, 675–702 (2004).
32. Goll, Y., Atlan, G. & Citri, A. Attention: the claustrum. *Trends Neurosci.* **38**, 486–495 (2015).
33. Mathur, B. N., Caprioli, R. M. & Deutch, A. Y. Proteomic analysis illuminates a novel structural definition of the claustrum and insula. *Cereb. Cortex* **19**, 2372–2379 (2009).
34. Puelles, L. in *The Claustrum: Structural, Functional, and Clinical Neuroscience* (eds Smythies, J. R. et al.) 119–176 (Academic, 2014).
35. Briscoe, S. D., Albertin, C. B., Rowell, J. J. & Ragsdale, C. W. Neocortical association cell types in the forebrain of birds and alligators. *Curr. Biol.* **28**, 686–696 (2018).
36. Buchanan, K. J. & Johnson, J. I. Diversity of spatial relationships of the claustrum and insula in branches of the mammalian radiation. *Ann. NY Acad. Sci.* **1225**, E30–E63 (2011).
37. Gabor, A. J. & Peele, T. L. Alterations of behavior following stimulation of the claustrum of the cat. *Electroencephalogr. Clin. Neurophysiol.* **17**, 513–519 (1964).
38. Renouard, L. et al. The supramammillary nucleus and the claustrum activate the cortex during REM sleep. *Sci. Adv.* **1**, e1400177 (2015).
39. Jackson, J., Karnani, M. M., Zemelman, B. V., Burdakov, D. & Lee, A. K. Inhibitory control of prefrontal cortex by the claustrum. *Neuron* **99**, 1029–1039 (2018).
40. Narikiyo, K. et al. The claustrum coordinates cortical slow-wave activity. Preprint at *bioRxiv* https://doi.org/10.1101/286773 (2018).
41. Siapas, A. G. & Wilson, M. A. Coordinated interactions between hippocampal ripples and cortical spindles during slow-wave sleep. *Neuron* **21**, 1123–1128 (1998).
42. McInnes, L., Healy, J. & Melville, J. UMAP: Uniform manifold approximation and projection for dimension reduction. Preprint at http://arxiv.org/abs/1802.03426 (2018).

Methods

Data reporting

No statistical methods were used to predetermine sample size. The experiments were not randomized and the investigators were not blinded to allocation during experiments and outcome assessment.

Animals

Lizards (*Pogona vitticeps*) of either sex, weighing 100–400 g, were obtained from our institute colony, selected for sex, size, weight, health status and wild-type colouring. Wild-type turtles (*T. scripta elegans* or *Chrysemys picta*) of either sex, weighing 200–400 g, were obtained from an open-air breeding colony (NASCO Biology). The animals were housed in our state-of-the-art animal facility.

All experimental procedures were performed in accordance with German animal welfare guidelines: permit no. V54-19c 20/15-F126/1005 delivered by the Regierungspraesidium Darmstadt (E. Simon).

Lizard surgery for chronic recordings

Twenty-four hours before surgery, the lizard was administered analgesics (butorphanol, 0.5 mg kg^{-1} subcutaneously; meloxicam, 0.2 mg kg^{-1} subcutaneously) and antibiotics (marbofloxacin, marbocyl, 2 mg kg^{-1}). On the day of surgery, anaesthesia was initiated with isoflurane, and maintained with isoflurane (1–4 vol%) after intubation. The lizard was placed in a stereotactic apparatus after ensuring deep anaesthesia (absence of corneal reflex). Body temperature during surgery was maintained at 32 °C using a heating pad and oesophageal temperature probe. Heart rate was monitored using a Doppler flow detector. The skin covering the skull was disinfected using 10% povidone-iodine solution before removal with a scalpel. A small (around 3 × 2-mm) craniotomy was then drilled posterior lateral to the parietal eye along the midline. The dura and arachnoid layers covering the forebrain were removed with fine forceps, and the pia was removed gently over the area of electrode insertion (dorsal or dorso-medial cortex). The exposed skull was covered with a layer of ultraviolet (UV)-hardening glue, and the bare ends of two insulated stainless steel wires were secured in place subdurally with UV-hardening glue to serve as the reference and ground.

For insertion of silicon probes, probes were mounted on a Nanodrive (Cambridge Neurotech) and secured to a stereotactic adaptor. On the day after the surgery, probes were slowly lowered into the tissue (about 0.9–1.2 mm). The brain was covered with Duragel followed by Vaseline. After connecting grounds, the skull, craniotomy and probes were secured with dental cement. After surgery, lizards were released from the stereotactic apparatus and left on a heating pad set to 32 °C until full recovery from anaesthesia.

In vivo electrophysiology

One week before surgery, lizards were habituated to a sleep arena for a minimum of two nights. One to two hours before lights off, the lizard was placed in the sleep arena, which was itself placed in a 3 × 3 × 3-m EM-shielded room. The animal was left to sleep and behave naturally overnight, and returned to its home terrarium 3–4 h after lights on. The animal then received food and water. Recordings were made from the cortex, anterior DVR (including claustrum) and/or posterior DVR of chronically implanted adult lizards. Electrodes were 32-channel silicon probes (50-μm pitch, 177-μm^2 surface area for each site; in 2 rows of 16 contacts).

Recordings were performed with a Cheetah Digital Lynx SX system and HS-36 headstages of unity gain and high input impedance (~1 TOhm). The headstage was connected with a headstage adaptor to a connector on the head, and a lightweight shielded tether cable connected the headstage to the acquisition system. Recordings were grounded and referenced against one of the reference wires. Signals were sampled at 32 kHz, with wide-band 0.1–9,000 Hz. Electrophysiological traces were typically low-pass filtered at 150 Hz with a 2-pole Butterworth filter for display.

Ibotenic acid lesion experiments

In preparation for claustrum lesion experiments we carefully removed, using fine forceps in anaesthetized animals, the pia overlaying the dorsal cortex and inserted a beveled quartz micropipette at an angle of 90° to the surface, to a depth of 1,050–1,150 μm from the surface, at appropriate anterior–posterior and medial–lateral coordinates to reach the centre of the claustrum. Ibotenic acid (400–600 nl; 5 μg μl^{-1} in PBS, pH 7.2) was injected at a rate of 50–100 nl min^{-1} (UMP3, World Precision Instruments). The injection pipette was retracted 3 min after the end of injection. Two silicon recording probes were subsequently positioned bilaterally, as described above, for DVR recordings. For sham claustrum lesions, we injected PBS alone (same methods and volumes) on the sham-lesion side. Recordings were carried out each night from one to six days after surgery. Effects of the lesions could already be observed 24 h after surgery. A week after each experiment, the animal was killed and its brain was sectioned and stained with Nissl for histological confirmation.

SWR delay calculation

Sharp waves were detected as described previously (template-based detection[3]). After independently detecting SWRs on probes in the aDVR and pDVR throughout the dataset, the delay between SWRs across probes was calculated by pairing SWRs on one probe with the SWR closest in time on the second probe. Pairs occurring more than 500 ms apart were ignored.

SWRs at the slow-wave sleep–REM sleep transition point

REM and slow-wave sleep periods and the timing of their transition were calculated as described previously[3]. Average SWR rates and amplitudes were calculated by averaging the values triggered on all slow-wave sleep–REM sleep transition points within 100-ms bins, and smoothing the resulting histogram with a Gaussian filter (s.d., 25 ms).

In ibotenic acid lesion experiments, sleep cycles were determined using median filtered β-band power (10–40 Hz, as above), for a 6-h period beginning 3 h after the recording start time. The time course of β was filtered above 0.001 Hz with a 2-pole Butterworth filter, and additionally smoothed with a Gaussian filter (s.d., 20 s). Periods of slow-wave sleep were conservatively defined as ones in which this signal was less than 1 s.d. below the mean. To avoid false sharp-wave detections in lesioned animals (which demonstrate reduced low-frequency power), sharp waves were detected by thresholding the voltage trace (1.5–2.5 s.d. below the mean) after low-pass filtering at 4 Hz with a 2-pole Butterworth filter. The threshold was adapted to each lesion experiment and was the same for both hemispheres within each experiment.

Sharp-wave shape statistics

For comparison with ex vivo and slice sharp waves, sharp waves detected in vivo were low-pass filtered at 20 Hz using a 2-pole Butterworth filter.

Ex vivo brain and slice preparations

Adult lizards or turtles were deeply anaesthetized with isoflurane, ketamine (60 mg kg^{-1}) and midazolam (2 mg kg^{-1}). After loss of the corneal reflex, the animals were decapitated and the heads were rapidly transferred into cooled ACSF solution (lizard: 126 mM NaCl, 3 mM KCl, 1.8 mM $CaCl_2$, 4 mM $MgCl_2$, 24 mM $NaHCO_3$, 0.72 mM NaH_2PO_4, 20 mM glucose, pH 7.4; turtle: 96.5 mM NaCl, 2.6 mM, KCl, 4 mM $CaCl_2$, 2 mM $MgCl_2$, 31.5 mM $NaHCO_3$, 20 mM glucose, pH 7.4) bubbled with carbogen gas (95% O_2, 5% CO_2).

Ex vivo intact subcortical slabs were prepared with iridectomy scissors, after isolation of the lizard brain. For slice preparation, coronal, horizontal or sagittal subcortical area slices (700 μm thick) were cut using a vibratome (VT 1200S, Leica) in ice-cold oxygenated ACSF. The slices were allowed to recover for at least 60 min and then submerged in a chamber filled with oxygenated ACSF (lizards: 126 mM NaCl, 3 mM

KCl, 1.8 mM $CaCl_2$, 1 mM $MgCl_2$, 24 mM $NaHCO_3$, 0.72 mM NaH_2PO_4, 20 mM glucose, pH 7.4; turtle: 96.5 mM NaCl, 2.6 mM KCl, 4 mM $CaCl_2$, 2 mM $MgCl_2$, 31.5 mM $NaHCO_3$, 20 mM glucose, pH 7.4) at 20–22 °C.

Ex vivo brain and slice physiology and SWR detection

During recordings, oxygenated ACSF (lizard: 126 mM NaCl, 3 mM KCl, 1.8 mM $CaCl_2$, 1.2 mM $MgCl_2$, 24 mM $NaHCO_3$, 0.72 mM NaH_2PO_4, 20 mM glucose, pH 7.4; turtle: 96.5 mM NaCl, 2.6 mM, KCl, 4 mM $CaCl_2$, 2 mM $MgCl_2$, 31.5 mM $NaHCO_3$, 20 mM glucose, pH 7.4) was constantly superfused at 18–20 °C (ex vivo) and 18–21 °C (slices) at 4 ml min^{-1}. LFPs were recorded using microelectrode arrays, silicon probes or glass pipettes filled with ACSF. The electrodes were carefully placed in the targeted areas with micromanipulators. Signals were low-pass filtered at 2 kHz and digitized at 20 kHz. For analysis of sharp waves, the traces were further low-pass filtered at 20 Hz using a 2-pole Butterworth filter. SWRs were detected at a threshold of 3× s.d. of the total signal. The detected events were visually scrutinized and manually rejected if they were erroneously detected. Events lasting less than 30 ms were also discarded as they were typically artefacts. For claustrum electrical-stimulation experiments, stimulation pulses lasted 50 µs and were delivered with bipolar electrodes. Multi-unit extracellular recordings in cortex were carried out with glass micropipettes filled with ACSF. Mini-slices were cut with a sharp razor blade and were 0.61–3.12 mm^2 in surface area.

CMOS–MEA experiments

The slices were placed over a high-density microelectrode array (3Brain AG) of 4,096 electrodes (electrode size, 21 × 21 µm; pitch, 81 µm; 64 × 64 matrix; 5.12 × 5.12-mm area). During recording, ACSF perfusion was interrupted to avoid movements of the slices and noise as a result of ACSF flux. Signals were sampled at 18 kHz with a high-pass filter at 1 Hz.

Saturating or damaged channels were detected as channels whose voltage crossed ± 500 µV and were removed from later analysis. Channel data were low-pass filtered at 20 Hz and *z*-scored, and troughs greater than 5(*z*) below the mean on the channel with the largest signal were taken as sharp waves. The signal ± 400ms from these peak times, on all channels, was taken as a SWR episode. For calculation of SWR latency, SWRs were averaged on each channel and the time that the average signal crossed 1(*z*) below the mean was taken as the start of the SWR on that channel. Latency was calculated relative to the time of the SWR of the earliest channel. Channels that did not cross 1(*z*) were considered maximum latency. The resulting latency image was filtered with a 3 × 3 median filter to remove the effect of bad channels, and upsampled by a factor of 10 for display.

Whole-cell patch-clamp recordings of DVR and claustrum neurons

Long-shank patch pipettes (6–8 MΩ) were pulled from borosilicate glass with a Sutter P1000 electrode puller. Pipettes were filled with internal solution (140mM K-gluconate, 4 mM NaCl, 14 mM phosphocreatine, 10 mM HEPES, 4 mM Mg–ATP, 0.3 mM Na–GTP, 4 mg ml^{-1} biocytin). Experiments were carried out on an upright Olympus BX61WI microscope with 5× and 40× water-immersion objectives and cells were patched under visual guidance. Excitatory and inhibitory postsynaptic currents were recorded in the voltage-clamp configuration with the same cell held at either −70 mV or +10 mV. Simultaneous patch-clamp and LFP recordings were carried out with an EPC10 Quadro amplifier (HEKA).

Pharmacology

Serotonin hydrochloride (0.1–30 µM), carbamoylcholine chloride (50 µM), noradrenaline bitartrate (25 µM), SKF38393 hydrobromide (10 µM), (R)-(+)-8-hydroxy-DPAT hydrobromide (2 µM), L-703,664 succinate (1 µM), CP 809101 hydrochloride (0.1 µM), LP44 (0.2 µM) and TTX (20 µM) were diluted to their final concentrations in ACSF (126 mM NaCl, 3 mM KCl, 1.8 mM $CaCl_2$, 1.2 mM $MgCl_2$, 24 mM $NaHCO_3$, 0.72 mM NaH_2PO_4, 20 mM glucose, pH 7.4). For slice experiments, drugs were continuously bath-applied after a baseline recording period of 5–20 min. For ex vivo experiments in Extended Data Fig. 8, TTX dissolved in ACSF was injected into the claustrum through a glass micropipette using a 10-ml syringe pressurizer (20–30 hPa for 15 min). For serotonin uncaging, RuBi-5HT (Abcam) (10 µM) was bath-applied, and white light (400–700 nm, 0.11 W cm^{-2}, TH4-200, Olympus) was turned on and off at chosen intervals (for example, 80 s).

We tested several metabotropic 5HTR agonists. Of those, the 5HTR-1D agonist L-703,664 best mimicked the effects of serotonin, consistent with the high expression of 5HTR-1D in glutamatergic neurons in the claustrum (Extended Data Fig. 5a). The 5HTR-7 agonist LP44 had no effect (Fig. 4f), which is also consistent with the low expression of 5HTR-7 in claustrum excitatory neurons. The 5HTR-2C agonist CP 809101 increased the rate but not the amplitude of SWRs.

scRNA-seq libraries

Adult male lizards (150–400 g) were deeply anaesthetized with isoflurane, ketamine (50 mg kg^{-1}) and midazolam (0.5 mg kg^{-1}) and decapitated. The head was immersed in ice-cold oxygenated ACSF (126 mM NaCl, 3 mM KCl, 2 mM $CaCl_2$, 4 mM $MgCl_2$, 24 mM $NaHCO_3$, 0.72 mM NaH_2PO_4, 20 mM glucose, pH 7.4). The brains were perfused to remove blood from the vasculature. The data shown originate from four libraries constructed from data from one male lizard (160 g, 20 months old).

Thereafter, the brain was removed and immersed in oxygenated ice-cold ACSF. The brain was embedded in 4% low-melting agarose, glued to the base of a vibratome (VT1200S, Leica) and immersed in ice-cold oxygenated ACSF, and 500-µm-thick sections were prepared (speed, 0.08 mm s^{-1}). The sections were individually inspected under a dissection microscope (Stemi 2000-C, Zeiss) and anatomical regions of interest were dissected (telencephalon, amDVR). These slices were cut with fine scissors (Fine Science Tools) into small cubes of tissue (around 500 × 500 × 500 µm).

These were transferred to dissociation buffer (20 U ml^{-1} papain, 200 U ml^{-1} DNase I, 25 µg ml^{-1} liberase TM, 1 µM TTX, 100 µM D-APV) and triturated with fire-polished, silanized glass pipettes of decreasing tip diameter (around 10 passes per pipette). After every pipette change the supernatant (dissociated cell suspension) was removed and filtered through a strainer with 100-µm mesh.

The pooled dissociated cell suspension was diluted to 20 ml (with Hibernate A −$CaCl_2$), transferred to a 50-ml reaction tube and filtered with a strainer with 40-µm mesh. Then 5 ml of 4% bovine serum albumin (BSA) in Hibernate A −$CaCl_2$ was added to the bottom of the tube with a long-stemmed glass pipette. The solution was spun in a centrifuge at 300*g* at 4 °C (lowest acceleration and brake) for 5 min. The supernatant was removed and the cell pellet resuspended in 20 ml of Hibernate A −$CaCl_2$. This procedure was repeated for a second-gradient clean-up. The pellet was then resuspended in an appropriate amount (50–200 µl) of Hibernate A −$CaCl_2$ −$MgCl_2$ and the cell concentration was measured with a Fuchs–Rosenthal cell-counting chamber (Brand).

The cell suspension was then diluted to 466 cells $µl^{-1}$ and used as input to half a chip (four samples) of the 10X Chromium system (Chemistry v.3) with a targeted cell recovery of 7,000 cells per sample. The library construction was performed according to the manufacturer's instructions.

The final four libraries were quantified using Qubit fluorometer (Thermo Fisher Scientific) and sequenced five times on a DNA sequencer (NextSeq 500, Illumina) with an average depth of 442,806,563 reads per library.

Analysis of transcriptomics data

Raw sequencing data were processed using Cellranger v.3.0 (10X Genomics). Raw reads were demultiplexed and filtered with the cellranger mkfastq function with default settings. To generate digital gene expression matrices, demultiplexed reads were aligned to the *Pogona*

genome with the cellranger count function, setting the force-cells parameter to 7,000. For reads alignment, we reannotated the *Pogona* genome (assembly 1.1.0, NCBI accession number GCF_900067755.1, 10 April 2017) using the same 3′-end MACE (massive analysis of cDNA ends) data and the approach described previously[11].

Digital gene expression matrices were analysed in R, using the Seurat v.3.0 package[14]. Cells were filtered by number of genes (more than 800 genes per cell) and percentage of mitochondrial genes (lower than 5%), yielding a total of 20,257 cells, with a median number of 2,278 transcripts and 1,349 genes per cell. Data were normalized by the total number of transcripts detected in each cell, and regressed by the number of genes and of transcripts (by setting vars.to.regress = c("nFeature_RNA", "nCount_RNA") in ScaleData function). Variable genes were identified after variance standardization from an estimate of the mean variance relationship (FindVariableFeature, method = "vst"), and the top 1,000 highly variable genes were used for principal component analysis. The first 30 principal components were used for Louvain clustering (FindClusters, resolution = 0.2) and for dimensionality reduction with UMAP[42] (RunUMAP with default settings).

After this first round of analysis, neuronal clusters (characterized by high expression of pan-neuronal markers, such as the synaptic protein *snap25*) were analysed again using the above procedure with the following settings: more than 800 genes per cell, 2,000 highly variable genes, 30 principal components, clustering resolution = 0.2. This led to the identification of 12 neuronal clusters. One cluster of doublets, recognized by the co-expression of markers of glutamatergic and GABAergic (γ-aminobutyric acid-producing) neurons, was removed, leaving 9,777 neurons. These were analysed again with the same parameters (but clustering resolution = 2) to yield 33 clusters (Extended Data Fig. 3).

From this neuronal dataset, we identified 4,054 pallial glutamatergic neurons (with more than 1,000 genes per cell) that co-expressed the vesicular glutamate transporters *slc17a7* and *slc17a6*. Further subclustering of these cells (analysis settings: 2,000 highly variable genes, 34 principal components, clustering resolution = 3) led to the identification of 29 clusters (Fig. 3a, Extended Data Fig. 3). To assign an identity to each of these clusters, we analysed the expression of marker genes with known tissue expression patterns[11]. This allowed us to define the pallial region to which each cluster belongs (for example, hippocampus for *zbtb20*-expressing clusters). Further annotation of cluster identities (Extended Data Fig. 3) was based on the expression of selective markers or combinations of marker genes, identified from the transcriptomics data. Note about gene nomenclature, all reptilian gene names are in lower case in the Article as per *Nature* style; however, in the extended data figures, reptilian gene names are in uppercase, according to convention.

Analysis of ion-channel and neurotransmitter-receptor genes

We mined the *Pogona* genome for the following gene families: noradrenaline, acetylcholine, serotonin and dopamine receptors; calcium, chloride, sodium and potassium channels; and GABA, glutamate, adenosine, cannabinoid, glycine and histamine receptors. This yielded 270 genes in total. Of these, 143 were kept for further analysis, because they were detected in at least 20% of the cells of at least one glutamatergic cluster (Extended Data Fig. 5a).

To calculate pairwise cluster correlations (Pearson correlations, Extended Data Fig. 5b), we used this set of 143 genes and average cluster expression data (calculated from normalized and log-transformed data with the AverageExpression function in the Seurat package). A distance matrix was calculated from the correlation matrix, and used for hierarchical clustering (R package hclust) with the Ward.D2 linkage method.

The gene expression matrix from above was transposed to calculate gene–gene correlations. The gene dendrogram was also calculated with hierarchical clustering and the Ward.D2 linkage method.

The heat map in Fig. 3h was generated from the matrix of 29 glutamatergic clusters (columns) and average expression of the 143 genes (rows). The data matrix was scaled by columns, and the heat map was plotted with the heatmap.2 function from the R package gplots. The dendrogram of glutamatergic clusters is based on Euclidean distance and Ward.D2 linkage.

Mapping of single-cell transcriptomes across species

To map *Pogona* single-cell transcriptomes on mouse single-cell data, we used the dataset from a previous study[13], which is available on the dropviz.org website. In this dataset, pallial glutamatergic neurons were sampled from three regions: 'hippocampus', 'frontal cortex' and 'posterior cortex'. These dissections encompass several cell types. For example, 'frontal cortex' includes the claustrum, and 'hippocampus' includes the subiculum and entorhinal cortex. Raw data were processed through the Seurat pipeline (normalization, scaling, selection of variable genes) and glutamatergic clusters and subclusters were selected, according to the cluster and subcluster identities provided previously (ref. [13] and dropviz.org). Subclusters were downsampled to a maximum number of 200 cells per subcluster, yielding a total of 17,455 cells.

Comparative analysis of *Pogona* and mouse was limited to one-to-one orthologues, according to the orthology annotations provided by Ensembl (*Pogona* assembly pv1.1 and mouse assembly GRCm38.p6, one-to-one orthologues downloaded on 1 May 2019). Of 13,273 one-to-one orthologues, 10,693 were detected in both the mouse and *Pogona* datasets and used for the comparative analysis.

The *Pogona* and mouse data were analysed jointly following the approach described previously[14]. In brief, after normalization and scaling, 1,500 highly variable genes were identified in each dataset. The union of these sets of variable genes was used for a joint canonical correlation analysis (CCA). The first 15 canonical components were then used to identify 2,626 transfer anchors; that is, pairs of cells with matching neighbourhoods (mutual nearest neighbours) in the two transcriptomics spaces (function FindTransferAnchors from Seurat). These anchors were then used to project *Pogona* cells (query dataset) on the mouse dataset (reference dataset), using the TransferData function from Seurat. The projection is based on a weighted classifier that assigns a classification score on the basis of the distance of each cell from the transfer anchors. Figure 3g represents the result of the classification, showing the fraction of single cells from each *Pogona* cluster that map to each of the mouse subclusters (mouse subclusters without matching lizard cells are not indicated in the figure).

The approach described above was also used to project the transcriptomes of turtle pallial glutamatergic cells onto the *Pogona* data (Extended Data Fig. 7a). The turtle data are from a previous study[11]. The comparison was based on 9,820 one-to-one orthologues detected in both species. For this analysis, the top 2,000 variable genes of each dataset were used for CCA. The first 25 canonical components were used to compute 3,406 transfer anchors.

Identification of *Pogona* brain areas with a potential role in brain-state regulation

Areas known to play a part in controlling brain state have been, over the past decades, identified in a number of mammalian species. Those areas can be identified by their location (for example, within the hypothalamus, midbrain or brainstem), their axonal projections and the neuroactive substances that their neurons contain and release (and thus potential marker genes). To our knowledge, no such description exists at present for the brain of the bearded dragon (*Pogona*), but anatomical studies of homologous areas have been performed in other reptilian species[43–55]. These references were used to identify relevant brain areas, including preoptic area, supramammillary nucleus[56] and tuberomammillary nucleus in the hypothalamus; ventral tegmental area, substantia nigra and periaqueductal grey in the midbrain; and lateral dorsal tegmental nucleus, locus coeruleus, subcoeruleus and

raphe nucleus in the brainstem. The location and identity of these areas were established in *Pogona* by immunohistochemistry and/or FISH using appropriate neuronal markers, combined with Nissl stains of brain sections. Tyrosine hydroxylase (a marker of catecholaminergic neurons) was used to identify preoptic area, ventral tegmental area, substantia nigra, periaqueductal grey and locus coeruleus; choline acetyltransferase was used to identify lateral dorsal tegmental nucleus; histamine was used to identify tuberomammillary nucleus; serotonin was used to identify raphe nucleus; and subcoeruleus identification was based on the prior identification of lateral dorsal tegmental nucleus and locus coeruleus and by the expression of *slc17a6* (vesicular glutamate transporter 2; a marker of glutamatergic neurons) by in situ hybridization (Extended Data Fig. 6a). The expression of *slcC17a6* by in situ hybridization was also used for the identification of supramammillary nucleus[56] (Extended Data Fig. 6a).

Pogona whole-brain images

Pogona brain reconstruction (Fig. 3i) was based on images obtained with a μCT scanner, and the 'surface' function of the Imaris software (Oxford Instruments). The boundaries of relevant nuclei were determined from consecutive serial histological sections. The serial images were aligned and assembled to three-dimensional (3D) volumes using the Voloom software, and then imported into Imaris and aligned with the 3D data. The boundaries of some areas identified by retrograde tracing were defined from GFP and Nissl staining patterns.

Immunohistochemistry and in situ hybridization

The lizards were deeply anaesthetized with isoflurane, ketamine (60 mg kg^{-1}) and midazolam (2 mg kg^{-1}) until loss of the foot-withdrawal reflex. Pentobarbital (10 mg kg^{-1}) was then administered by intraperitoneal injection. After loss of the corneal reflex, the lizard was perfused transcardially with cold PBS (1.47×10^{-3} M KH_2PO_4, 8.10×10^{-3} M $Na_2HPO_4 \cdot 12H_2O$, 2.68×10^{-3} M KCl, 1.37×10^{-1} M NaCl) followed by 4% paraformaldehyde (PFA) in PBS. The brain samples were post-fixed with 4% PFA–PBS for 16 h at 4 °C and subsequently immersed in 30% sucrose for 24 h at 4 °C. The brain area was sectioned coronally (60 μm) with a microtome at −24 °C. The sections were permeabilized for 30 min at room temperature in blocking solution (PBST: PBS with 0.3% Triton X-100 and 10% goat serum) and incubated with primary antibodies (anti-GFP, A10262, Invitrogen, chicken, 1:1,000; hippocalcin, ab24560, Abcam, rabbit, 1:1,000; ChAT, AB144P, Merck, goat, 1:100; mTH, 22941, ImmunoStar, mouse, 1:100; rabTH, AB152, Merck, rabbit, 1:200; histamine, 22939, ImmunoStar, rabbit, 1:100; serotonin, MAB352, Merck, rat, 1:100) in blocking solution overnight at 4 °C. After washing with PBST three times, the samples were incubated with secondary antibodies conjugated with appropriate secondary antibodies (1:500, all from Invitrogen) in blocking solution for 4 h at room temperature, followed by three washes with PBST. Some slices were counterstained with NeuroTrace 435/455 blue-fluorescent Nissl stain (N21479, Invitrogen, 1:200) in PBS for 2 h at room temperature. After rinsing with PBS, the samples were mounted with Dako Fluorescence Mounting Medium (S3023, Dako) or Roti-Mount FluorCare DAPI (HP20.1, Carl Roth). Images were acquired using a confocal system or fluorescent microscopy at 10×, 20× or 40×. Chromogenic in situ hybridization and dual colorimetric in situ hybridization were performed following the protocols previously described[11].

Fluorescent in situ hybridization by RNAscope

The lizards were deeply anaesthetized as described above. After loss of corneal reflex, the animals were killed by decapitation. Brains were dissected out immediately, embedded in OCT on a dry-ice ethanol bath and stored at −80 °C. Fresh frozen brains were sectioned at 25 μm on a Thermo Fisher Scientific CryoStar NX70 cryostat and placed onto SuperFrost-coated (Thermo Fisher Scientific) slides. Some slides were stored at −80 °C after air-drying. RNAscope hybridization was performed according to the manufacturer's instructions. We used the RNAscope Multiplex Fluorescent assay (Advanced Cell Diagnostics) for fresh-frozen sections. Target genes and probe catalogue numbers were Pv-CHAT-C2, 522631-C2; Pv-SLC17A6-C1, 529431-C1. Fluorescent Nissl was used for counterstaining. Slides were mounted with ProLong Gold Diamond Antifade Mountant (P36970, Thermo Fisher Scientific). Images were acquired with a digital slide scanner (Pannoramic MIDI II, 3DHISTECH) at 20× magnification.

Tract tracing

The lizards were anaesthetized as described for in vivo recordings. Extensive preliminary searches for useful AAV serotypes for reptilian brains and for appropriate incubation conditions were carried out by L. Pammer[22]. The tracers (rAAV2-retro-CAG-GFP, 37825-AAVrg; rAAV2-retro-hSyn-EGFP, 50465-AAVrg; AAV9-CB7.CI.mCherry.WPRE.RBG, 105544-AAV9; all from Addgene, https://www.addgene.org) were injected into one or two forebrain locations (for example, dorsomedial cortex, DVR, amDVR, and so on). Four to six weeks later, the animals were deeply anaesthetized as described above, and after loss of corneal reflex, the animals were killed by decapitation. Brains were dissected out, processed for histology, sectioned and imaged. The data presented come from 18 of 30 injected brains. The remaining 12 brains were rejected either because the viral injections failed or because the injections were not sufficiently specific. Targeting specific regions in the brain of *Pogona* and *Trachemys* is difficult because the brain is loosely contained in the cranial cavity and its position relative to the cranium and reliable landmarks is thus variable: the brain floats in CSF, attached by cranial nerves. As a consequence, there are no reliable stereotactic coordinates based on cranium landmarks. The lateral ventricles are large. The external appearance of the forebrain also lacks reliable landmarks (for example, blood vessels or sulci). Finally, these animals are not standardized species, bred over generations to reduce variability.

Note that, because rAAV2-retro does not infect all neuronal types equally[23], the results from negative retrograde labelling should be confirmed with other methods. Conversely, the connectivity estimated with the tracers we used is likely to be underestimated.

Statistics and reproducibility

Unless stated otherwise, data are mean ± s.e.m. For comparisons of two groups we performed a two-tailed unpaired *t*-test, two-tailed paired *t*-test, Mann–Whitney rank-sum test or Wilcoxon signed-rank test, as appropriate (all two-sided). For multiple comparisons we performed a Bonferroni test. Significance was determined at the 0.05 α level for all statistical tests. For box plots (Fig. 4d): margins are 25th and 75th percentiles; red, median; whiskers, boundaries before outliers; outliers (+) are values beyond 1.5× interquartile range from the box margins. Experiments were repeated independently several times with similar results, with numbers of repetitions as follows: Fig. 1b–e: 7 times; Fig. 2a–c: 4 times; Fig. 2e: 13 times (amDVR) and 9 times (plDVR); Fig. 3: 4 times (a, b, d–h) and 10 times (c); Fig. 4a–c: 3 times; Extended Data Fig. 1a–d: 7 times; Extended Data Fig. 1h: 3 times; Extended Data Fig. 2b: 15 times; Extended Data Fig. 2g, i: 12 times; Extended Data Fig. 2h, j: twice; Extended Data Fig. 3f: 3 times; Extended Data Fig. 4a: 3 times; Extended Data Fig. 4b: 13 times (amDVR) and 9 times (plDVR); Extended Data Fig. 6a–c: 3 times (for all except for c5–7, for which experiments were reproduced once in 5 experiments) (see Fig. 3 legend); Extended Data Fig. 7b: 3 times; Extended Data Fig. 7c: 5 times; Extended Data Fig. 7d: 4 times; Extended Data Fig. 7e, g: 3 times; Extended Data Fig. 8a, e, f: 4 times; Extended Data Fig. 8b–d: 4 times; Extended Data Fig. 9a–d: twice (a, b) and 3 times (c) (claustrum lesions (d) were confirmed in all these experiments); Extended Data Fig. 10a, b: twice (a) and 3–4 times (b).

Reporting summary

Further information on research design is available in the Nature Research Reporting Summary linked to this paper.

Data availability

Sequencing data have been deposited in the NCBI Sequence Read Archive: BioProjects PRJNA591493 (lizard) and PRJNA408230 (turtle). Links to those archives and to analysis code can be found at: https://brain.mpg.de/research/laurent-department/software-techniques.html. Data are also available from the corresponding author on request.

43. Moreno, N., Domínguez, L., Morona, R. & González, A. Subdivisions of the turtle *Pseudemys scripta* hypothalamus based on the expression of regulatory genes and neuronal markers. *J. Comp. Neurol.* **520**, 453–478 (2012).
44. Medina, L., Smeets, W. J., Hoogland, P. V. & Puelles, L. Distribution of choline acetyltransferase immunoreactivity in the brain of the lizard *Gallotia galloti*. *J. Comp. Neurol.* **331**, 261–285 (1993).
45. Bruce, L. L. & Neary, T. J. Afferent projections to the ventromedial hypothalamic nucleus in a lizard, *Gekko gecko*. *Brain Behav. Evol.* **46**, 14–29 (1995).
46. Bruce, L. L. & Neary, T. J. Afferent projections to the lateral and dorsomedial hypothalamus in a lizard, *Gekko gecko*. *Brain Behav. Evol.* **46**, 30–42 (1995).
47. Ebner, F. F. in *Evolution of Brain and Behavior in Vertebrates* (eds Masterton, R. B. et al.) 115–167 (Taylor & Francis, 1976).
48. Font, C., Lanuza, E., Martinez-Marcos, A., Hoogland, P. V. & Martinez-Garcia, F. Septal complex of the telencephalon of lizards: III. Efferent connections and general discussion. *J. Comp. Neurol.* **401**, 525–548 (1998).
49. Hoogland, P. V. & Vermeulen-Vanderzee, E. Efferent connections of the dorsal cortex of the lizard *Gekko gecko* studied with *Phaseolus vulgaris*–leucoagglutinin. *J. Comp. Neurol.* **285**, 289–303 (1989).
50. Smeets, W. J. & Steinbusch, H. W. Distribution of noradrenaline immunoreactivity in the forebrain and midbrain of the lizard *Gekko gecko*. *J. Comp. Neurol.* **285**, 453–466 (1989).
51. Smeets, W. J., Hoogland, P. V. & Voorn, P. The distribution of dopamine immunoreactivity in the forebrain and midbrain of the lizard *Gekko gecko*: an immunohistochemical study with antibodies against dopamine. *J. Comp. Neurol.* **253**, 46–60 (1986).
52. ten Donkelaar, H. J., Bangma, G. C., Barbas-Henry, H. A., de Boer-van Huizen, R. & Wolters, J. G. The brain stem in a lizard, *Varanus exanthematicus*. *Adv. Anat. Embryol. Cell Biol.* **107**, 1–2 (1987).
53. ten Donkelaar, H. J. in *The Central Nervous System of Vertebrates* Vol. 1–3 (eds Nieuwenhuys, H. et al.) 1315–1524 (Springer, 1998).
54. Wolters, J. G., ten Donkelaar, H. J., Steinbusch, H. W. & Verhofstad, A. A. Distribution of serotonin in the brain stem and spinal cord of the lizard *Varanus exanthematicus*: an immunohistochemical study. *Neuroscience* **14**, 169–193 (1985).
55. Wolters, J. G., ten Donkelaar, H. J. & Verhofstad, A. A. Distribution of catecholamines in the brain stem and spinal cord of the lizard *Varanus exanthematicus*: an immunohistochemical study based on the use of antibodies to tyrosine hydroxylase. *Neuroscience* **13**, 469–493 (1984).
56. Pedersen, N. P. et al. Supramammillary glutamate neurons are a key node of the arousal system. *Nat. Commun.* **8**, 1405 (2017).

Acknowledgements We thank K. Steele and A. Schwartzlose for help with serotonin immunocytochemistry and neural tract tracing; E. Northrup and G. Wexel for veterinary care; T. Klappich for reptile care; S. Junek, F. Vollrath and C. Polisseni for help with imaging and microscopy; G. Tushev for help with genome reannotation; E. Desfilis for help with lizard neuroanatomy; and members of the Laurent laboratory for help and comments. The work was funded by the Max Planck Society, the European Research Council under the European Union's Seventh Framework Programme (FP7/2007-2013) (ERC grant agreement no. 322705), the European Research Council under the European Union's Horizon 2020 research and innovation programme (ERC grant agreement no. 834446) and the DFG (CRC1080) (G.L.); postdoctoral fellowships from the JSPS (SPD and for research abroad) and from the Kanae Foundation for the promotion of medical science (H.N.); and an EMBO long-term fellowship (ALTF 421-2017) (L.A.F.).

Author contributions H.N. and L.A.F. contributed equally and have equal right to list themselves first in bibliographic documents. H.-H.L. and M.A.T. also contributed equally. Project conception, H.N., L.A.F. and G.L.; animal surgery, M.K., H.N. and L.A.F.; electrophysiology, H.N., L.A.F. and S.R.; pharmacology, H.N., R.K. and L.A.F.; scRNA-seq, T.G.F., D.H., A.M. and M.A.T.; bioinformatics, M.A.T. and D.H.; tracing, anatomy and histology, L.A.F., H.-H.L., R.K., T.G.F., A.A. and M.K.; experimental design, data interpretation and analysis, H.N., L.A.F., H.-H.L., M.A.T., T.G.F., D.H., S.R. and G.L.; project management and supervision, G.L.; manuscript writing, G.L., with input from all co-authors.

Competing interests The authors declare no competing interests.

Additional information

Supplementary information is available for this paper at https://doi.org/10.1038/s41586-020-1993-6.

Correspondence and requests for materials should be addressed to G.L.

Peer review information *Nature* thanks Michael Lazarus and the other, anonymous, reviewer(s) for their contribution to the peer review of this work.

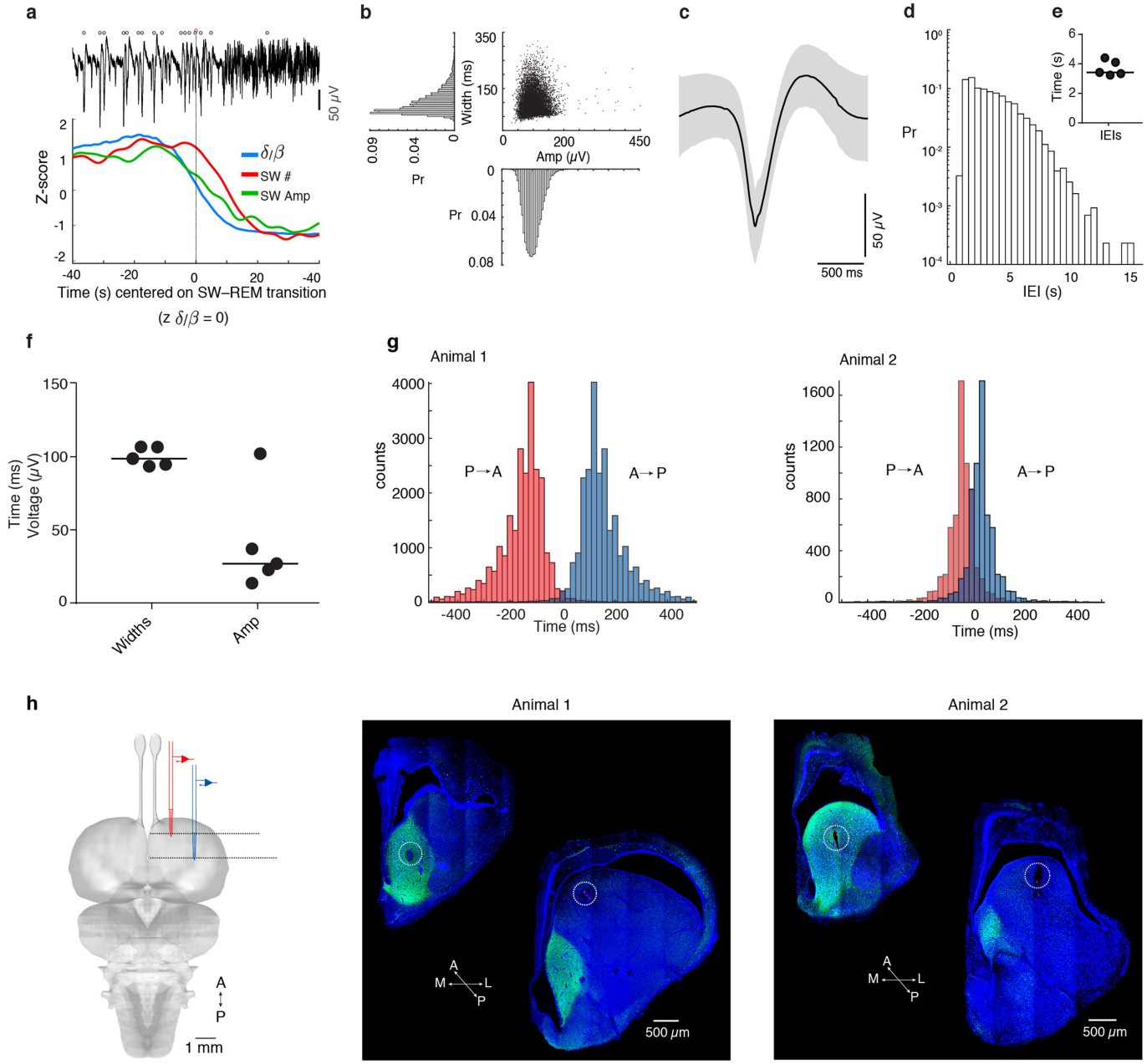

Extended Data Fig. 1 | Further description of SWR statistics and propagation in vivo. a, The amplitude and frequency of sharp waves vary as the animal transitions between slow-wave and REM sleep. Top, illustrative LFP trace (<150 Hz) showing a decrease in sharp-wave amplitude and frequency around the slow-wave–REM transition point. Open circles indicate detected sharp waves[3] (see Methods). Data in **a**–**d** are from the same animal and a single night, and correspond to the recording in Fig. 1 (anterior recording site, red). Statistics are based on $n = 11{,}123$ sharp waves. **b**, Distribution of sharp-wave width (measured at half peak amplitude) and peak amplitude from the animal in **a** and Fig. 1. Pr, probability. **c**, Average sharp-wave trace ± 1 s.d. (grey) calculated over $n = 11{,}123$ sharp waves. **d**, Inter-event interval (IEI) for sharp waves recorded during slow-wave sleep. The *y* axis (probability) is on a logarithmic scale. **e**, **f**, Summary of data recorded over five nights from two animals. Each circle represents the mean of one night; black line shows the median. **e**, Mean inter-event intervals during slow-wave sleep. **f**, Mean sharp-wave width and amplitude ($n = 8{,}055$–$13{,}494$ sharp waves per night). **g**, Delay distributions of sharp waves in anterior (or posterior) DVR, triggered on simultaneously recorded posterior (or anterior) DVR. Sharp waves from three nights (animal 1; $n = 24{,}501$ sharp waves) and two nights (animal 2; $n = 13{,}070$ sharp waves). **h**, Locations of simultaneous recording sites in the aDVR (circles). Left, schematic of recording configuration. Middle and right, confocal images highlighting the recording sites, as identified by electrolytic lesions and DiI dye that was applied to the back of the silicon probes. Post hoc staining with an antibody against hippocalcin was used to determine the borders of the claustrum (see Fig. 3).

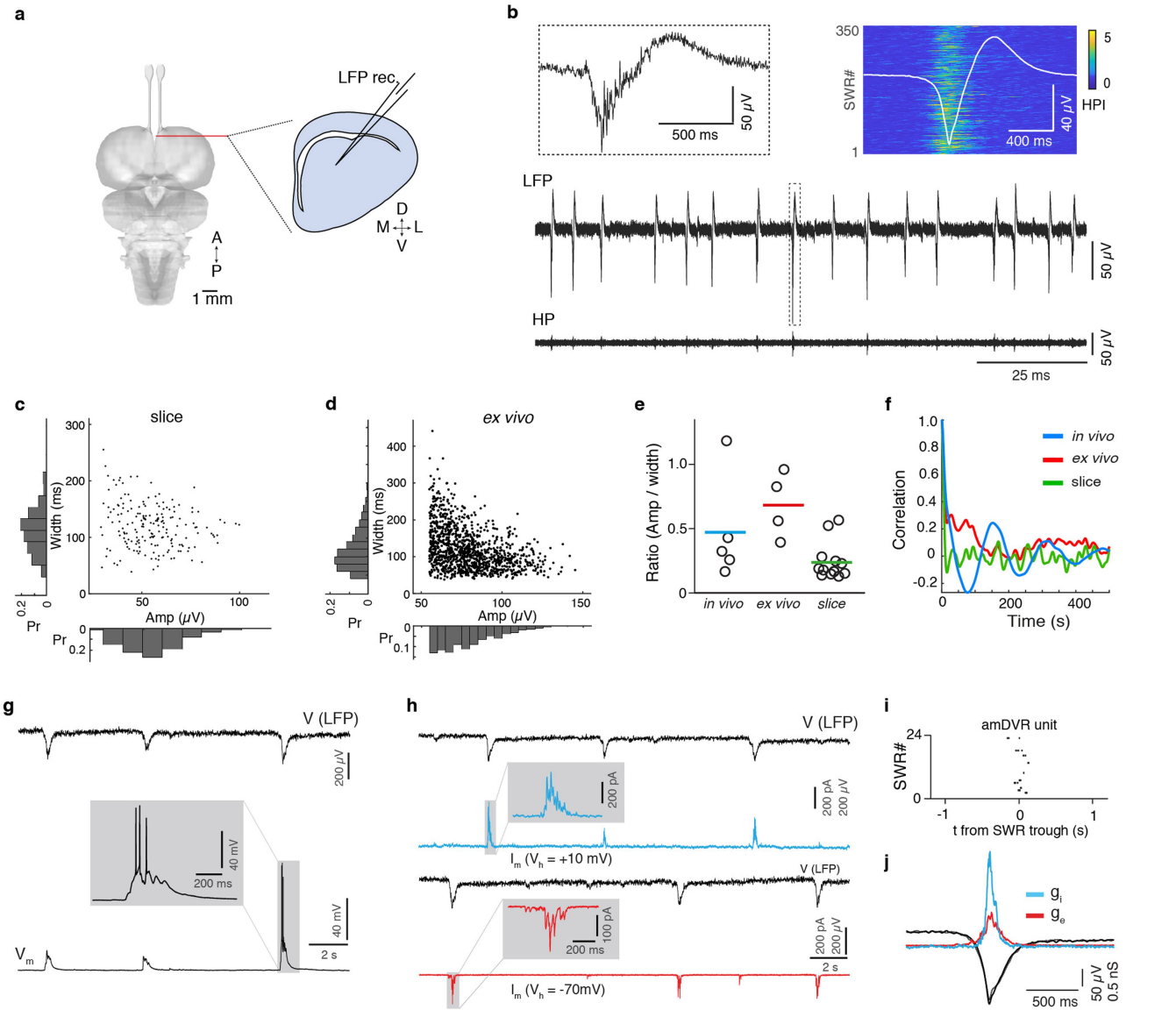

Extended Data Fig. 2 | Comparison of SWR statistics across preparations and recording conditions. a, Slice preparation (see Methods) for field-potential recordings. **b**, Spontaneous sharp waves (LFP; <150 Hz) and corresponding ripples (high-pass (HP) band; 70–150 Hz) in the amDVR. Insets: top left, magnification of the SWR marked with a dotted box; top right, 350 ripples; high-pass signal intensity (HPI) >70 Hz aligned on trough of sharp wave (overlaid as average). **c**, Distribution of amplitude (x) and width (y, full width at half maximum) of SWR events in a representative DVR slice. **d**, Distribution of SWR amplitude and width (as in **c**) in a representative ex vivo preparation. **e**, Ratio of amplitude (μV) to width (ms); $n = 5$ sleep epochs from 3 animals (in vivo; blue), 4 ex vivo brains (red) and 12 slices (green). Lines show the mean. **f**, Autocorrelation function of sharp-wave times, showing that the characteristic rhythmic modulation of sharp-wave generation (which is due to the alternation of slow-wave sleep and REM sleep with a 2–3 min period) in sleeping animals is absent from both ex vivo brain preparations and slice preparations ($n = 5$ sleep epochs from 3 animals (in vivo), 4 ex vivo brains and 12 slices). **g**, Whole-cell patch-clamp recording (in current-clamp mode) of a DVR neuron (V_m), together with LFP recording in a neighbouring region (V(LFP)) with a glass micropipette. Note the simultaneous depolarization of the neuron and SWRs, and moderate neuronal depolarization that gives rise to occasional firing (three action potentials here). The experiment was repeated with 12 neurons. **h**, Whole-cell patch-clamp recording of an amDVR neuron in voltage-clamp mode, held at depolarized (blue) and hyperpolarized (red) holding potentials (V_h). Note the volleys of excitatory (red) and inhibitory (blue) currents at each SWR (LFP), and the near absence of synaptic input in between. **i**, Spike times of a patched amDVR neuron in relation to sharp waves. Note the locking to the sharp-wave trough ($t = 0$), and the absence of firing otherwise ($n = 2$ amDVR neurons). **j**, Mean excitatory (g_e) and inhibitory (g_i) conductances ($n = 20$ and 21 events, respectively). The black and grey lines show averaged sharp waves recorded with inhibitory and excitatory conductances, respectively. Traces are aligned on the sharp-wave trough.

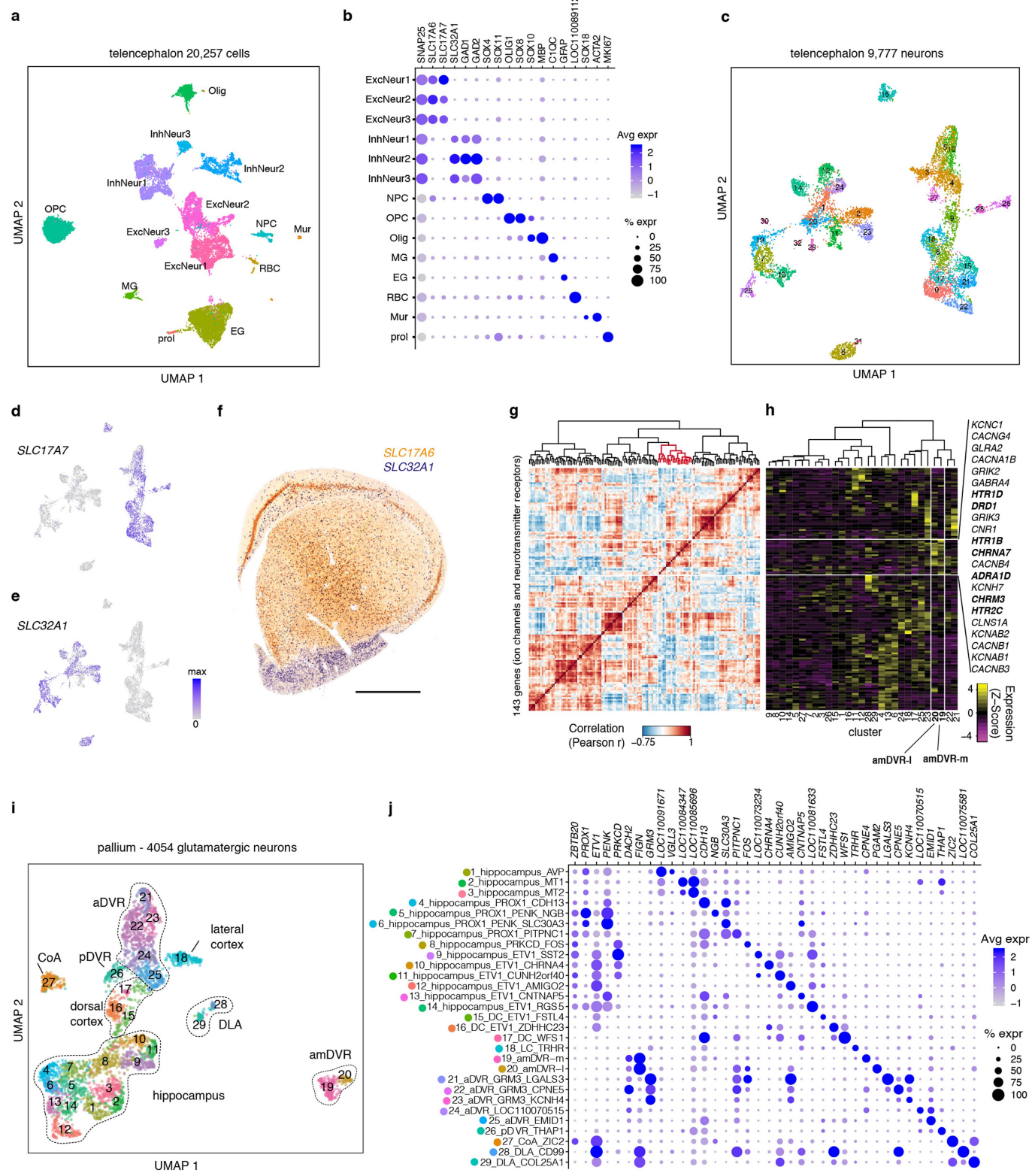

Extended Data Fig. 3 | See next page for caption.

Extended Data Fig. 3 | Additional single-cell transcriptomic characterization. a, UMAP[42] representation of 20,257 *Pogona* telencephalic cells, colour-coded by cluster. EG, ependymoglial cells; ExcNeur, excitatory neurons; InhNeur, inhibitory neurons; MG, microglia; mur, mural cells; NPC, neural progenitor cells; olig, oligodendrocytes; OPC, oligodendrocyte progenitor cells; prol, proliferating cells; RBC, red blood cells. **b**, Dot plot showing the expression of canonical cell markers (rows) across telencephalic cell clusters (columns). The size of the dot corresponds to the percentage of cells in a cluster in which the gene has been detected, and the colour represents the expression level. **c**, UMAP representation of 9,777 lizard telencephalic neurons, colour-coded by cluster. **d**, **e**, UMAP representations of glutamatergic (*slc17a7*) and GABAergic (*slc32a1*) neurons in the telencephalon dataset. **f**, Double colorimetric in situ hybridization in a frontal section through the anterior *Pogona* forebrain. Scale bar, 1 mm. *slc32a1* (blue) labels GABAergic neurons in the subpallium and scattered GABAergic neurons that have migrated from subpallium to pallium. *slc17a6* (orange) labels glutamatergic neurons in the pallial region. **g**, Ordered matrix of pairwise Pearson correlations between the expression of 143 ion-channel and neurotransmitter-receptor genes detected in this glutamatergic pallial dataset from *Pogona* (see Extended Data Fig. 5). The dendrogram (top) is based on correlation coefficients and Ward.D2 linkage; red indicates a gene module with enriched expression in the amDVR. **h**, Average expression, in the 29 glutamatergic *Pogona* clusters, of the 143 genes in **g** (and Extended Data Fig. 5). Genes with enriched expression in the amDVR are listed on the right, with relevant neurotransmitter receptor genes in bold. **i**, UMAP representation of 4,054 lizard pallial glutamatergic neurons, colour-coded by cluster (same as in Fig. 3a). **j**, Dot plot showing the expression of specific cluster markers (rows) in the 29 pallial glutamatergic clusters (columns). The size of the dot corresponds to the percentage of cells in a cluster in which the gene has been detected, and the colour represents the expression level.

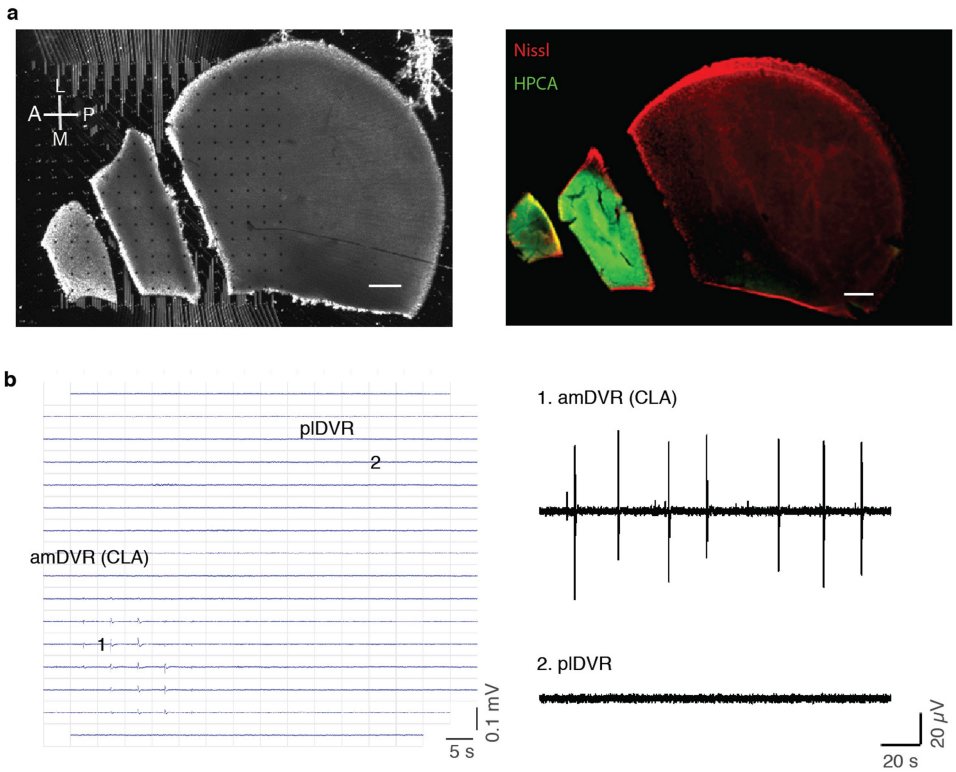

Extended Data Fig. 4 | Mini-slices of the DVR and localization of SWR generation. a, Left, recording configuration of mini-slices of the DVR on a planar 252-channel microelectrode array. Dots represent electrodes. Right, post hoc immunostaining of the mini-slices. Red, Nissl; green, hippocalcin. **b**, Left, spatial distribution of SWR waveforms as recorded from the mini-slices in **a**. Right, illustrative LFP traces recorded from the amDVR or claustrum (1) and plDVR (2) (see recording positions on the microelectrode array on the left). In conclusion, SWRs occur spontaneously in the amDVR, and are absent from the plDVR once it is disconnected from the amDVR (claustrum).

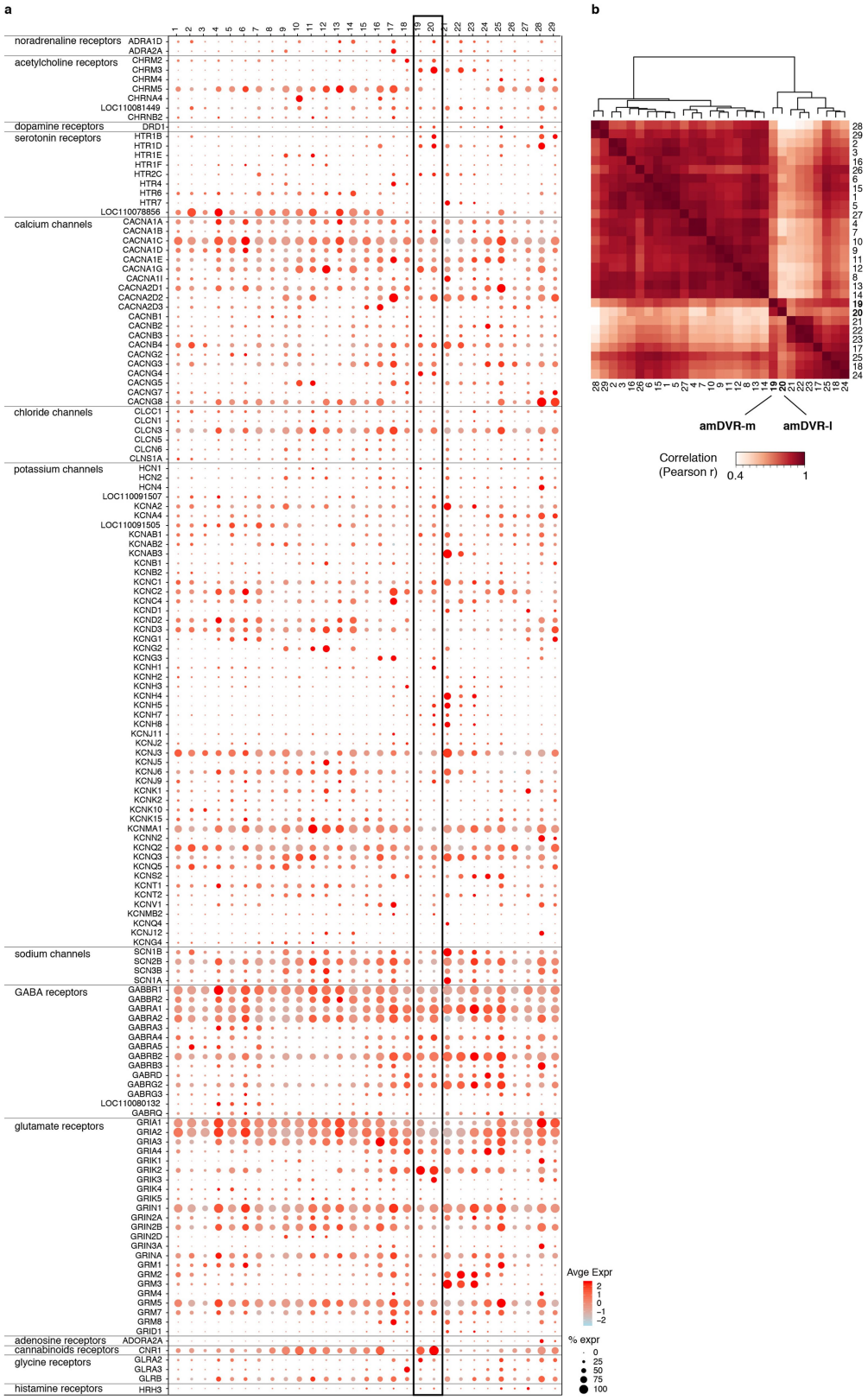

Extended Data Fig. 5 | Ion-channel and neurotransmitter-receptor mRNAs in the glutamatergic cell clusters of the *Pogona* telencephalon. a, Dot plot showing expression of ion-channel and neurotransmitter-receptor genes (rows) in *Pogona* glutamatergic clusters (columns 1–29). The plot shows only genes that were detected in at least 20% of the cells of at least one cluster. The size of the dot corresponds to the percentage of cells in a cluster in which the gene has been detected, and the colour represents the expression level. Clusters 19 and 20 (box) correspond to the amDVR or claustrum. They differ by the expression of some acetylcholine- and serotonin-receptor subtypes (see also Fig. 3h). **b**, Ordered pairwise Pearson correlation matrix of cluster transcriptomes, calculated from the expression of the ion-channel and neurotransmitter-receptor genes in **a**. This gene set is sufficient to distinguish the amDVR clusters (19 and 20) from all of the others. The dendrogram is based on Pearson correlations and Ward.D2 linkage.

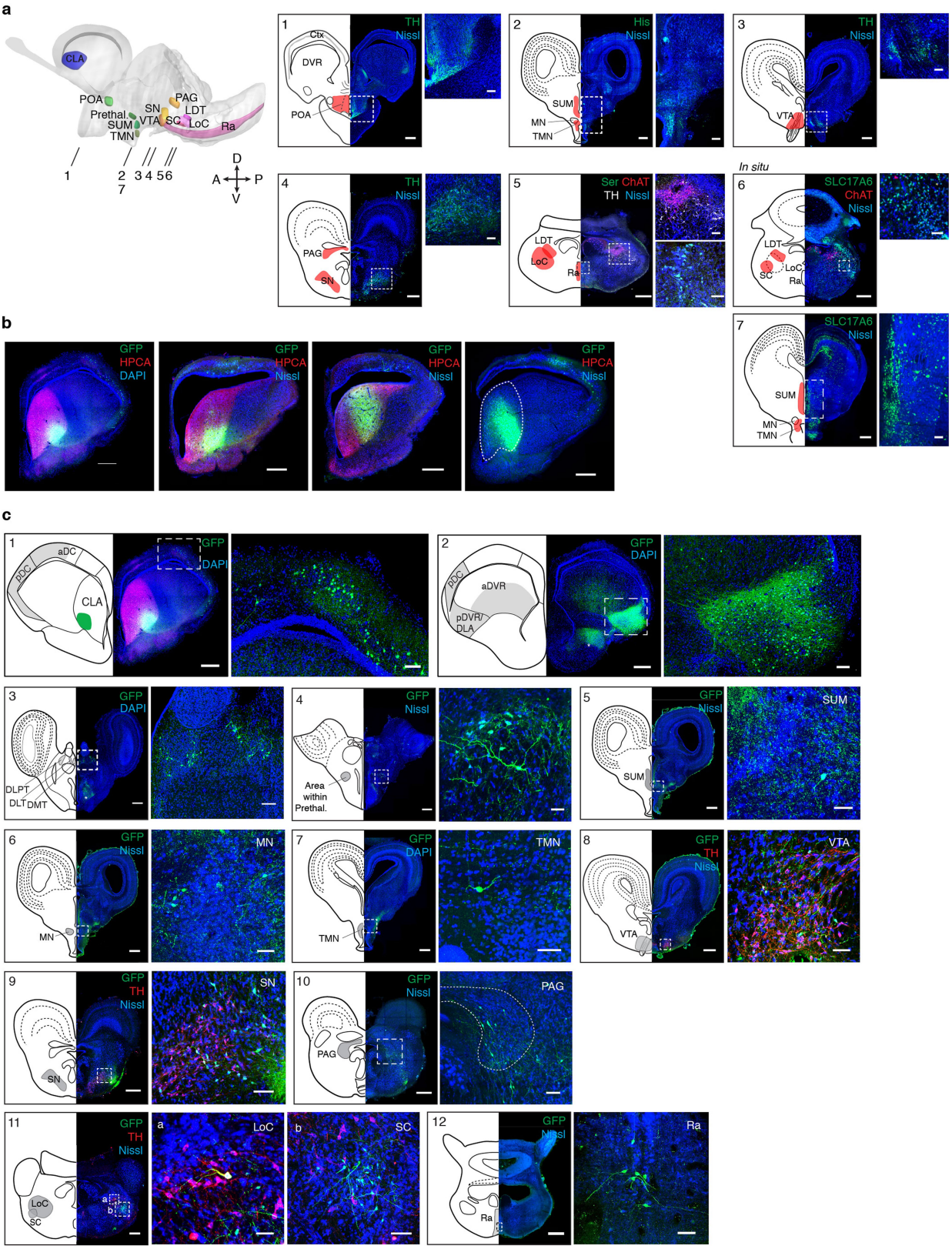

Extended Data Fig. 6 | See next page for caption.

Extended Data Fig. 6 | Identification of potential regulatory areas of brain states and distribution of GFP-labelled neurons after injection of rAAV2-retro into the claustrum. a, Left, schematic of the *Pogona* brain in sagittal view, showing the regions defined by immunohistochemistry, in situ hybridization and retrograde tracing. Numbers 1–7 indicate the levels of the transverse sections that are shown on the right. Right (panels 1–7), micrographs and corresponding schematic representations of relevant areas (in red), identified by immunohistochemistry, in situ hybridization and Nissl staining. Scale bars, 500 µm. Far right of panels 1–7, magnified views of area(s) delineated as box(es) in the corresponding photomicrographs. Scale bars, 100 µm. **b**, Identification of rAAV2-retro injection sites. Scale bars, 500 µm. The red channel is not shown in the rightmost image. **c**, Illustrative examples of retrograde labelling of claustrum connectivity, in transverse sections. Panels 1, 2, inputs to claustrum revealed by rAAV2-retro injection in the claustrum. Panel 1, injection site in lateral claustrum. The claustrum is indicated by anti-hippocalcin immunostain (pink). Note retro-labelled cells in the anterior dorsal cortex (box, magnified at right). Panel 2, same brain as in 1, but a more posterior section. The labelled region in the box is the dorsal lateral amygdala. Panels 3–12, representative images illustrating the distribution of GFP-labelled neurons in the DLPT, DLT, DMT, prethalamus, SUM, mammillary nucleus (MN), TMN, VTA, SN, PAG, LoC and SC, with projections to the claustrum. Abbreviations as in Fig. 3. The catecholaminergic neuron marker tyrosine hydroxylase (TH) was used to indicate the location of the VTA, SN and LoC. Scale bars, 500 µm. Scale bars for magnified areas: DLPT, DLT, DMT, prethalamus, SUM, MN, TMN, VTA, LoC, 50 µm; SN, PAG, SC, 100 µm.

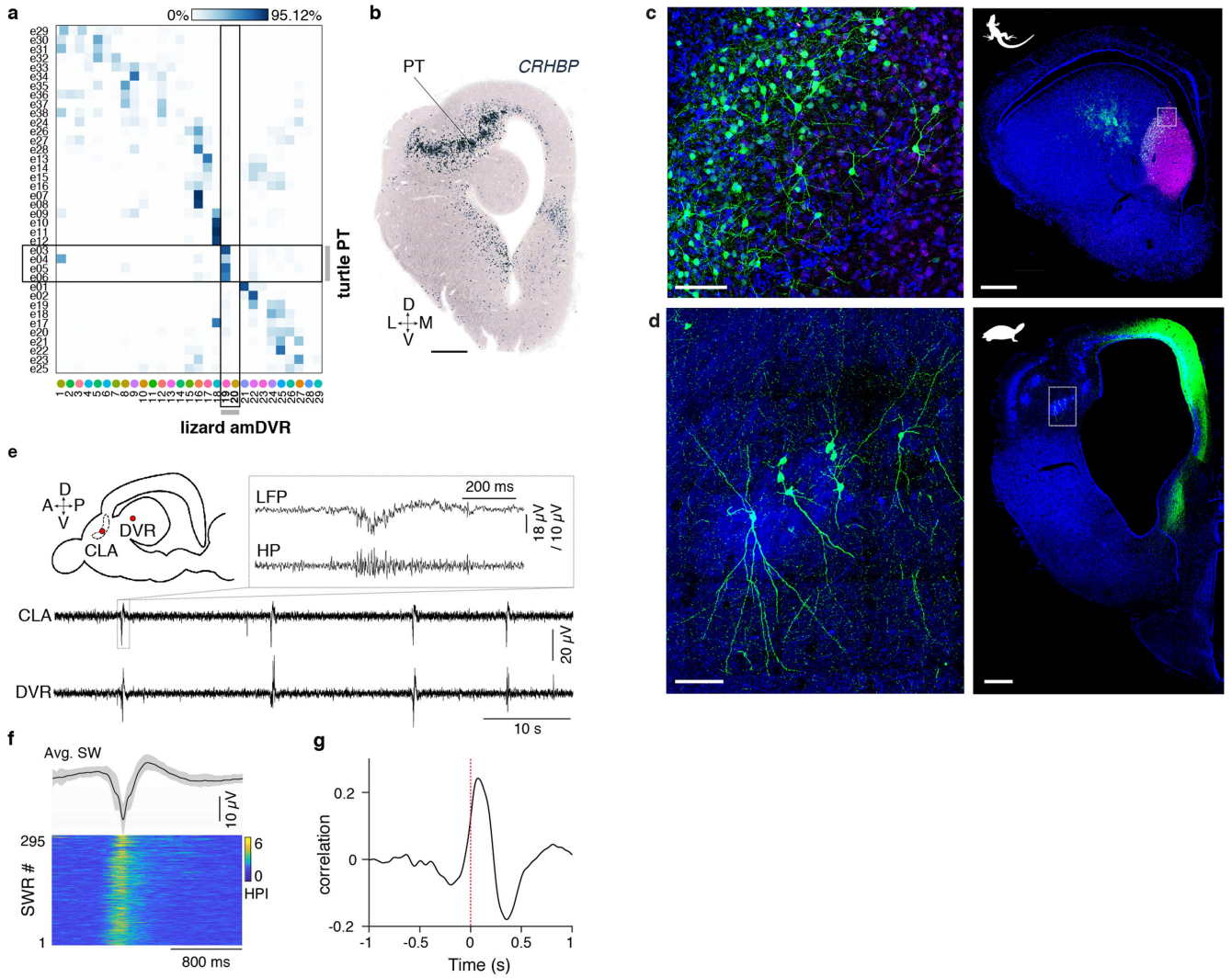

Extended Data Fig. 7 | The claustrum of lizard and turtle differ in position and architectonics, but are both autonomous sources of SWRs. **a**, Transcriptomic similarity between turtle and lizard clusters, measured as the fraction of single cells that mapped from the turtle pallium dataset to the *Pogona* clusters (Methods). Note that the turtle cell clusters e03–e06 (pallial thickening; PT) map to the lizard cluster 19 (amDVR or claustrum). Turtle data and clusters are from a previous study[11]. **b**, In situ hybridization in an anterior transverse section, showing expression of the pallial thickening marker gene *crhbp*. Scale bar, 500 µm. **c**, Architectonics of the lizard claustrum. Right, retrograde labelling of claustrum neurons by rAAV2-retro injected into the aDVR. Left, magnification of the boxed area on the right (in the claustrum). Note the disordered distribution of multipolar neurons. Pink colour shows anti-hippocalcin immunostaining. Scale bars, 100 µm (left); 500 µm (right). **d**, Architectonics of the turtle claustrum. Right, retrograde labelling of claustrum neurons by rAAV2-retro injected into the dorso-medial cortex. Left, magnification of the boxed area on the right. Note the arrangement of bipolar neurons within the pallial thickening layer (see also **b** for layering of pallial thickening). Scale bars, 100 µm (left); 500 µm (right). **e**, Spontaneous sharp waves recorded simultaneously in the claustrum and the DVR in turtle slice preparation. The red dots in the schematic indicate recording sites. Note sharp wave (LFP) and ripple in the high-pass (HP) band. **f**, Bottom, 295 successive spontaneous ripples (high-pass signal intensity (HPI) > 70 Hz) aligned on the trough of each sharp wave. Top, average of 295 sharp waves aligned on waveform troughs. Grey shading represents s.d. **g**, Representative cross-correlogram of LFP traces recorded simultaneously from the claustrum and the DVR (with claustrum as reference), showing the sharp waves from the DVR trailing those from the claustrum.

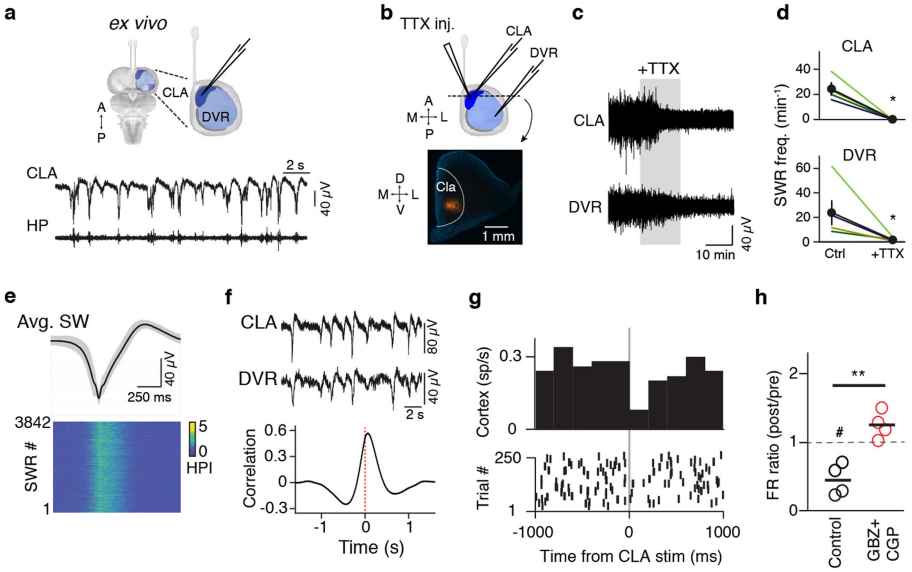

Extended Data Fig. 8 | SWR recordings and stimulation experiments with lizard ex vivo brain preparations. a–**f**, Experiments in ex vivo brain preparation after cortex removal. **a**, Top, ex vivo brain preparation. Bottom, spontaneous SWRs recorded in the claustrum (<150 Hz) (top trace); HP: 70–150-Hz filtered LFP, showing ripples (bottom trace). **b**, Local pressure injection of 20 μM TTX into the claustrum and post hoc assessment of injection with Evans blue (transverse section at the bottom, red). **c**, Injection of TTX into the claustrum (shading) silences sharp-wave activity in the claustrum, but also (indirectly) in the DVR. **d**, Analysis of four experiments as in **c**. The filled circles represent mean ± s.e.m. Claustrum: $^*P = 0.029$, $T = 26$ (two-sided Mann–Whitney rank-sum test); DVR: $^*P = 0.029$, $T = 26$ (two-sided Mann–Whitney rank-sum test). **e**, Top, average trace and s.d. (shading) from 3,842 sharp waves recorded from the claustrum of an ex vivo forebrain (alignment on trough). Bottom, HPI (>70 Hz) aligned on sharp-wave trough, showing ripple alignment. **f**, Top, simultaneous recordings from ipsilateral claustrum and DVR in an ex vivo preparation. Bottom, cross-correlation between simultaneous recordings in ipsilateral claustrum and DVR, showing that the claustrum precedes the DVR by around 100 ms. **g**, Peristimulus time histogram for multi-unit activity in the cortex, in response to activation of ipsilateral claustrum in an intact ex vivo forebrain. The experiment was carried out in normal ACSF at room temperature in the presence of 30 μM serotonin to suppress spontaneous SWRs in the claustrum and 50 μM carbachol to raise cortex excitability. The claustrum stimulus consisted of a single 50-μs electrical pulse, delivered with a bipolar electrode. Cortex multi-unit activity was recorded with a glass micropipette. **h**, Change in cortical firing rate (FR) measured in a 200-ms bin after the claustrum stimulus versus a 200-ms bin before the stimulus (as in **g**, on each side of $t = 0$). The control column plots the firing-rate ratio measured in the experiment in **g**, and the GBZ + CGP column plots the results of the same experiment after addition of the GABA receptor antagonists gabazine (GBZ; 5 μM) and CGP52432 (CGP; 2 μM); $n = 4$ ex vivo brains from 3 animals each. The control experiment shows that stimulation of the claustrum has an immediate and reliable inhibitory effect on the cortex (#: significantly different from baseline, $P = 0.017$, $t_3 = 4.8$ (two-sided paired t-test)). The stimulation experiment in GABA receptor antagonists shows that stimulation of the claustrum now slightly excites the cortex (**: significantly different from control, $P = 2.0 \times 10^{-3}$, $t_6 = -5.22$ (two-sided Student's t-test)), suggesting that projections from the claustrum both activate and inhibit cortical neurons, probably via direct excitatory projections and indirect inhibitory ones through interneurons (see rodent experiments in a previous study[39]). Short horizontal lines indicate mean.

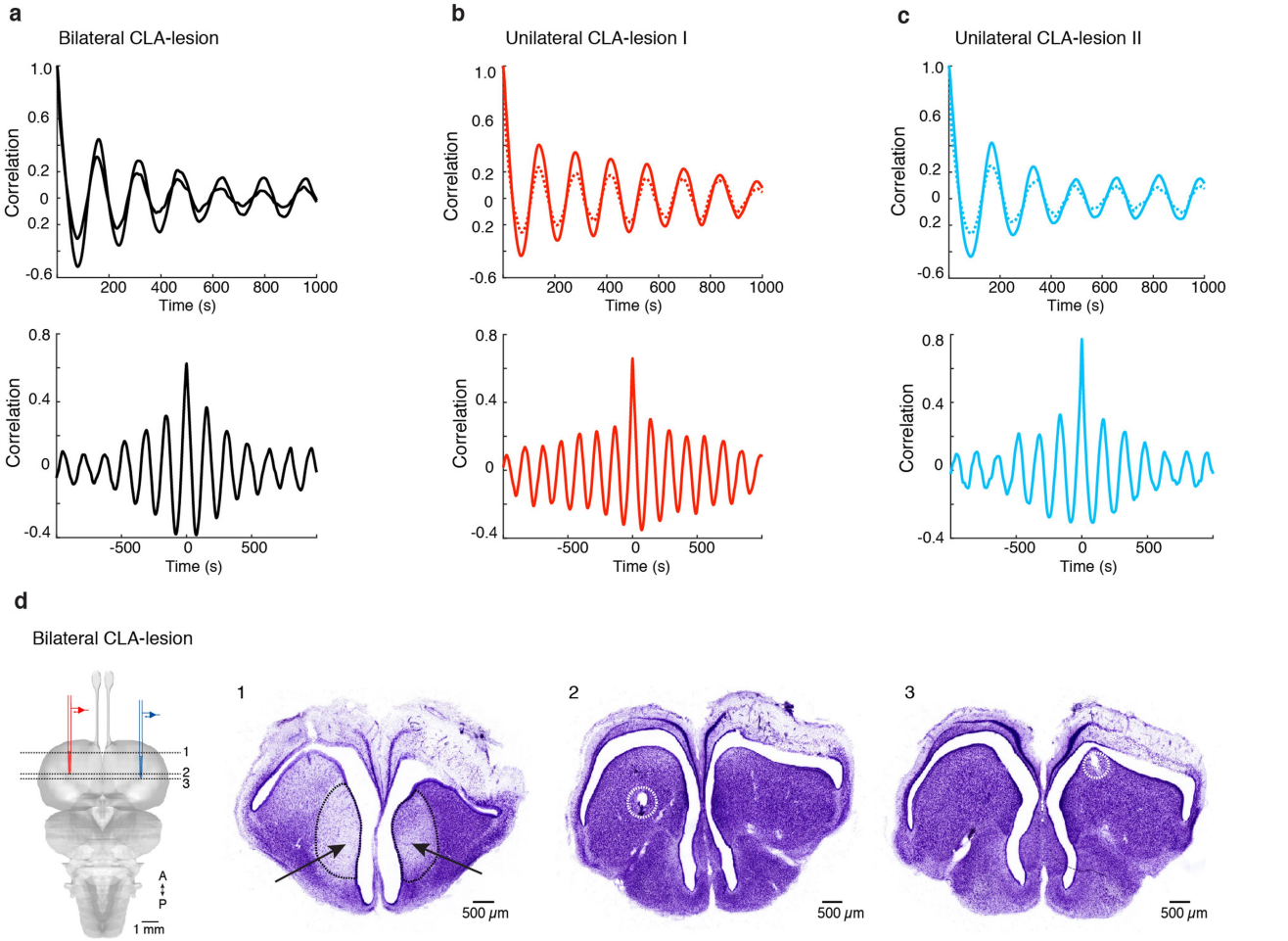

Extended Data Fig. 9 | Further analysis of in vivo ibotenic-acid-induced lesion experiments in sleeping *Pogona*. **a**, Autocorrelation (top) and cross-correlation (bottom) of β-band activity in the left and right DVR during sleep in an animal with bilateral claustrum lesions (lesions are shown in **d**). Note that a periodic sleep rhythm (period of around 3 min here) remains after claustrum lesions and therefore does not seem to depend on claustrum integrity. **b**, **c**, Same as **a**, but with unilateral ibotenic-acid-induced lesion in two animals (I and II). The non-lesioned (sham) side was injected with the same volume of PBS vehicle but without ibotenic acid. Dotted line, sham; solid line, lesion. **d**, Nissl stains (1–3) of transverse sections of the brain of animals with bilateral lesions (shown also in Fig. 4b), at levels indicated in the schematic on the left. Note the claustral lesions (arrows in 1), which are visible as cell-body loss, and the recording sites in left (2) and right (3) DVRs (dotted circles).

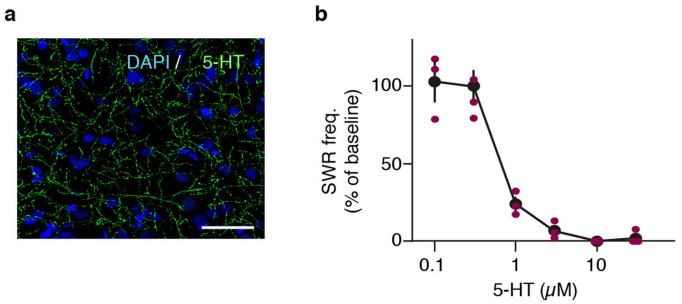

Extended Data Fig. 10 | Further data on serotonergic projections to claustrum and their effects on the generation of sharp-wave ripples. **a**, Transverse section of claustrum double-labelled with DAPI (blue, nuclei) and serotonin (axonal fibres) antibodies. Note the dense meshwork of serotonergic fibres. Scale bar, 50 µm. **b**, Frequency of spontaneous SWRs in claustrum mini-slices as a function of superfused serotonin concentration. Red circles represent individual experiments (slices). Black points and lines are mean ± s.e.m.

nature research

Corresponding author(s): Gilles Laurent

Last updated by author(s): Nov 27, 2019

Reporting Summary

Nature Research wishes to improve the reproducibility of the work that we publish. This form provides structure for consistency and transparency in reporting. For further information on Nature Research policies, see Authors & Referees and the Editorial Policy Checklist.

Statistics

For all statistical analyses, confirm that the following items are present in the figure legend, table legend, main text, or Methods section.

n/a	Confirmed	
☐	☒	The exact sample size (*n*) for each experimental group/condition, given as a discrete number and unit of measurement
☐	☒	A statement on whether measurements were taken from distinct samples or whether the same sample was measured repeatedly
☐	☒	The statistical test(s) used AND whether they are one- or two-sided *Only common tests should be described solely by name; describe more complex techniques in the Methods section.*
☒	☐	A description of all covariates tested
☐	☒	A description of any assumptions or corrections, such as tests of normality and adjustment for multiple comparisons
☐	☒	A full description of the statistical parameters including central tendency (e.g. means) or other basic estimates (e.g. regression coefficient) AND variation (e.g. standard deviation) or associated estimates of uncertainty (e.g. confidence intervals)
☐	☒	For null hypothesis testing, the test statistic (e.g. *F*, *t*, *r*) with confidence intervals, effect sizes, degrees of freedom and *P* value noted *Give P values as exact values whenever suitable.*
☒	☐	For Bayesian analysis, information on the choice of priors and Markov chain Monte Carlo settings
☒	☐	For hierarchical and complex designs, identification of the appropriate level for tests and full reporting of outcomes
☒	☐	Estimates of effect sizes (e.g. Cohen's *d*, Pearson's *r*), indicating how they were calculated

Our web collection on statistics for biologists contains articles on many of the points above.

Software and code

Policy information about availability of computer code

Data collection	in vivo data were collected using Cheetah (Neuralynx) and ex vivo and slice recordings were collected with pClamp 10.5 (Molecular Devices), patchmaster v2x90 (Heka), BrainWave v.4.4.1. (3Brain), and MC_Rack (Multichannel Systems). For the brain reconstruction we used µCT scanner and Imaris software (Oxford Instruments), confocal images were taken with Zen 2.1 software (Carl Zeiss).
Data analysis	Custom written code (MatLab 2016a-2017b) was used anayze physiological data. Raw sequencing data were processed using Cellranger v3.0 (10xGenomics), and digital gene expression matrices were analyzed in R, using the Seurat v3.0 package. Reconstruced brain images were analyzed with the Voloom 3.0 (micro Dimensions) and Imaris 9.2 (Oxford Instruments).

For manuscripts utilizing custom algorithms or software that are central to the research but not yet described in published literature, software must be made available to editors/reviewers. We strongly encourage code deposition in a community repository (e.g. GitHub). See the Nature Research guidelines for submitting code & software for further information.

Data

Policy information about availability of data

All manuscripts must include a data availability statement. This statement should provide the following information, where applicable:

- Accession codes, unique identifiers, or web links for publicly available datasets
- A list of figures that have associated raw data
- A description of any restrictions on data availability

All data and code will be available in full upon request. Accession codes for sequencing/transcriptomic data are provided.

Field-specific reporting

Please select the one below that is the best fit for your research. If you are not sure, read the appropriate sections before making your selection.

☒ Life sciences ☐ Behavioural & social sciences ☐ Ecological, evolutionary & environmental sciences

For a reference copy of the document with all sections, see nature.com/documents/nr-reporting-summary-flat.pdf

Life sciences study design

All studies must disclose on these points even when the disclosure is negative.

Sample size	No statistical tests were used to predetermine sample sizes. The amount of brain samples used for each experiment was chosen based on previous experience with this specific type of experiments and commonly used sample sizes in this field of research, taking into account the unusual nature and limited availability of the animal species studied.
Data exclusions	Experiments with off-target placement of electrodes or viral infection were excluded from our analyses. For transcriptomic analyses, only cells were considered for which the number of detected genes was >800 genes/cell (> 1000 for glutamatergic neurons), and the percentage of mitochondrial genes <5%/cell, as detailed in the methods. The exclusion criteria was pre-established.
Replication	We observed similar results which satisfied the same statistical criteria across experiments and we could replicate all our results.
Randomization	Animals were not assigned to groups, and were selected based on weight, health and temperament (for in vivo experiments). Randomization was not relevant for our study.
Blinding	Investigators were not blinded to group allocation during data collection and analysis. Our study was mostly observational in nature with the exception of pharmacological experiments (Fig. 6), comparing the effect of neuromodulators, ibotenic acid, and TTX injections on sleep EEG and SWR production. Measurement of the effect were fully automated, and blinding was thus not relevant for our study.

Reporting for specific materials, systems and methods

We require information from authors about some types of materials, experimental systems and methods used in many studies. Here, indicate whether each material, system or method listed is relevant to your study. If you are not sure if a list item applies to your research, read the appropriate section before selecting a response.

Materials & experimental systems

n/a	Involved in the study
☐	☒ Antibodies
☒	☐ Eukaryotic cell lines
☒	☐ Palaeontology
☐	☒ Animals and other organisms
☒	☐ Human research participants
☒	☐ Clinical data

Methods

n/a	Involved in the study
☒	☐ ChIP-seq
☒	☐ Flow cytometry
☒	☐ MRI-based neuroimaging

Antibodies

Antibodies used	Standard, commercially available antibodies were used. Primary antibodies were anti-GFP (A10262, invitrogen, chicken, 1:1000); anti-Hippocalcin (ab24560, abcam, rabbit, 1:1000); anti-ChAT-choline acetyltransferase (AB144P, Merk, goat, 1:100); antiTH-tyrosine hydroxylase (22941, Immunostart, mouse, 1:100 or AB152, Merk, rabbit, 1:200); anti-Histamine (22939, Immunostart, rabbit, 1;100); and anti-Serotonin (MAB352, Merk, rat, 1:100); secondary antibodies were Donkey or Goat anti-rabbit, chicken, goat, mouse, or rat, conjugated with Alexa-488, 568, 647 (A21206, A21208, A11039, A11011, A11057, A11004, A31573, A21247, A31571, all from Invitrogen, all 1:500)
Validation	The manufacturer validated the antibody by Western dot and dot blot. IHC validation was performed in our laboratory, testing various concentrations on lizard tissue.

Animals and other organisms

Policy information about studies involving animals; ARRIVE guidelines recommended for reporting animal research

Laboratory animals	Lizards (Pogona vitticeps, either sex, adult (100-400g)) were bred in-house or obtained from external breeders. Turtles (Trachemys scripta elegans or Chrysemys picta, either sex, adult (200-400g)) were obtained from an open-air breeding colony (NASCO Biology, WI, USA), and all species used were housed in our state-of-the-art animal facility.

Wild animals	This study did not involve wild animals.
Field-collected samples	This study did not involve field-collected samples.
Ethics oversight	All experimental procedures were performed in accordance with German animal welfare guidelines: permit #V54- 19c 20/15-F126/1005 delivered by the Regierungspraesidium Darmstadt, Germany (Dr. E. Simon).

Note that full information on the approval of the study protocol must also be provided in the manuscript.